Cell Reports

Resource

# Phosphoproteomic Analysis across the Yeast Life Cycle Reveals Control of Fatty Acyl Chain Length by Phosphorylation of the Fatty Acid Synthase Complex

## Graphical Abstract

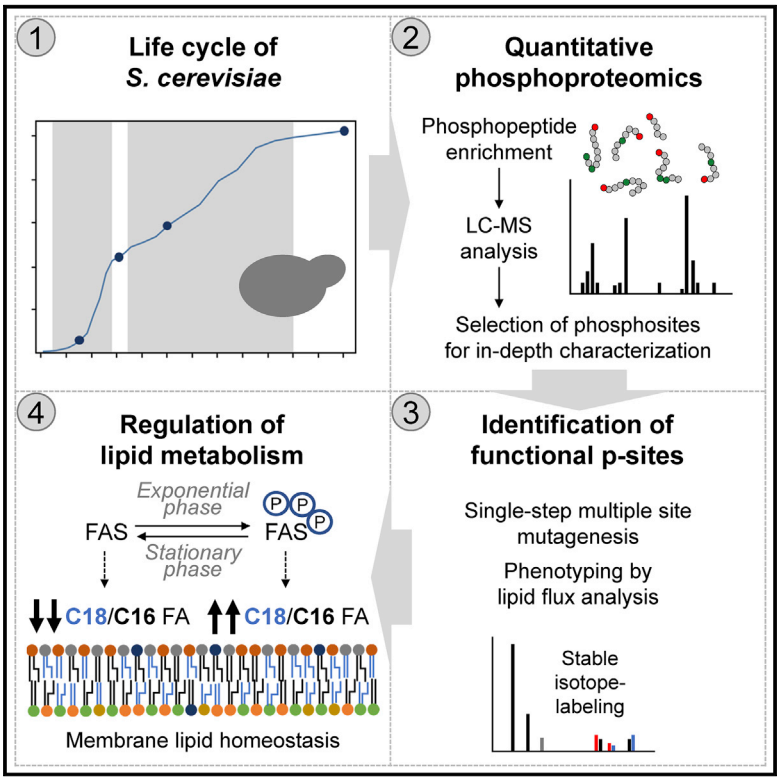


## Highlights

- Time-series analysis of 10,794 phosphosites across the yeast life cycle
- 50 lipid metabolic proteins are differentially phosphorylated
- Lipidomics flux analysis reveals functional phosphosites in Cds1 and Cho1
- Fatty acyl chain length is controlled by phosphorylation of the FAS complex

## Authors

Fernando Martínez-Montañés, Albert Casanovas, Richard R. Sprenger, ..., Martin Hermansson, Ole N. Jensen, Christer S. Ejsing

## Correspondence

cse@bmb.sdu.dk

## In Brief

Martínez-Montañés et al. generate a comprehensive phosphoproteomic resource of the yeast life cycle and find that numerous lipid metabolic proteins are phosphoregulated. By genome editing and lipidomics flux analysis, the authors show that fatty acyl chain length is controlled by phosphorylation of the FAS complex.

Martínez-Montañés et al., 2020, Cell Reports *32*, 108024
August 11, 2020 
https://doi.org/10.1016/j.celrep.2020.108024

CellPress

Cell Reports

CellPress
OPEN ACCESS

Resource

# Phosphoproteomic Analysis across the Yeast Life Cycle Reveals Control of Fatty Acyl Chain Length by Phosphorylation of the Fatty Acid Synthase Complex

Fernando Martínez-Montañés,[1] Albert Casanovas,[1] Richard R. Sprenger,[1] Magdalena Topolska,[1] David L. Marshall,[2] Marta Moreno-Torres,[1] Berwyck L.J. Poad,[2] Stephen J. Blanksby,[2] Martin Hermansson,[1] Ole N. Jensen,[1] and Christer S. Ejsing[1,3,4,*]

[1]Department of Biochemistry and Molecular Biology, VILLUM Center for Bioanalytical Sciences, University of Southern Denmark, Odense, Denmark

[2]Central Analytical Research Facility, Institute for Future Environments, Queensland University of Technology, Brisbane, QLD 4000, Australia

[3]Cell Biology and Biophysics Unit, European Molecular Biology Laboratory, Heidelberg, Germany

[4]Lead Contact

*Correspondence: cse@bmb.sdu.dk

https://doi.org/10.1016/j.celrep.2020.108024

## SUMMARY

The ability to remodel lipid metabolism under changing conditions is pivotal for cellular functionality and homeostasis. Here, we characterize the regulatory landscape of phosphorylation-based signaling events across the life cycle of *Saccharomyces cerevisiae* and determine its impact on the regulation of lipid metabolism. Our data show that 50 lipid metabolic proteins are differentially phosphorylated as cells transit between different physiological states. To identify functional phosphosites, we devised a strategy where multiple phosphosites are simultaneously mutated into phosphomimetic or phosphodeficient alleles and mutants are phenotyped by in-depth lipidomics flux analysis. This uncovers functional phosphosites in the phosphatidate cytidylyltransferase Cds1, the phosphatidylserine synthase Cho1, and Fas2, the α-subunit of the fatty acid synthase (FAS) complex. Furthermore, we show that the fatty acyl chain length produced by FAS is governed by phosphorylation. Overall, our work demonstrates a vital role for phosphoregulation of lipid metabolism and provides a resource to investigate its molecular underpinnings.

## INTRODUCTION

Cellular lipid metabolism is essential for all organisms, as it impinges on membrane structure and dynamics, energy homeostasis, and signal transduction events (Holthuis and Menon, 2014). At its core is an extensive metabolic network that produces and interconnects the metabolism of thousands of lipid molecules that together constitute the lipidome and span simple fatty acyl (FA) chains as well as more complex glycerophospholipids, glycerolipids, sphingolipids, and sterol lipids (Ejsing et al., 2009). Most of the key enzymes involved in lipid biosynthesis and turnover have been identified (Futerman and Hannun, 2004; Harayama and Riezman, 2018; Henry et al., 2012; Vance and Vance, 2004), and a range of molecular mechanisms underlying lipid homeostasis (Ernst et al., 2016) and modulation of individual lipid metabolic activities are known (DeBose-Boyd and Ye, 2018; Zechner et al., 2012). By contrast, how cells regulate and coordinate multiple lipid metabolic pathways to meet the requirements of specific cellular states and adapt the lipidome comprehensively is unclear.

This systems-level regulation of lipid metabolism is particularly important for the ability of cells to adapt to changes in nutrient availability and other environmental cues. For example, cell proliferation requires extensive lipid metabolic remodeling in order to produce an adequate complement of lipid building blocks that supports membrane expansion and cell growth (Gray et al., 2004; Zhu and Thompson, 2019). Similarly, when nutrient availability is scarce, lipid metabolism is remodeled in order to mobilize FA chains from storage lipids and use these for energy production in quiescence. In higher eukaryotes, the ability to switch between the states of proliferation and quiescence is important during cell differentiation and tissue development (Coller, 2019). Furthermore, dysregulation of the underlying pathways or defects in systems controlling metabolic switching between cell growth and proliferation are often linked to diseases such as cancer (Locasale and Cantley, 2011).

To achieve regulation of lipid metabolism at the systems level, dedicated signaling pathways sense changes in intracellular and environmental conditions and mediate the necessary responses. These signaling pathways are perhaps best annotated in the yeast *Saccharomyces cerevisiae* (Conrad et al., 2014; Ewald, 2018) and are surprisingly well conserved in higher eukaryotes (González and Hall, 2017; Lin and Hardie, 2018; Rinaldi et al., 2010). Yeast is easily cultured in many different conditions, and the controlled analysis of at least five different physiological states is readily possible when using rich media (Figure 1A)

(Gray et al., 2004; Hanscho et al., 2012). The first state is termed the ''lag phase,'' where quiescent cells upon nutrient availability adapt cellular processes in order to prepare for the second ''exponential growth phase,'' where cells proliferate rapidly using fermentative metabolism and produce ethanol as a biproduct. Here, the high concentrations of nutrients, including glucose, amino acids, and phosphate, prompt increased activity of numerous signaling pathways, including the cyclic-AMP-dependent protein kinase (PKA) pathway, the target of rapamycin complex 1 and 2 (TORC1 and TORC2) pathways, and the phosphate-sensing and response (PHO) pathway. These pathways collectively impinge on the Cdc28 controlled cell-cycle signaling pathway driving cell growth and division (Jiménez et al., 2013; Mizunuma et al., 2013; Moreno-Torres et al., 2015). Upon glucose exhaustion, the AMP-activated kinase (AMPK) pathway is activated and the PKA pathway is attenuated (Hedbacker and Carlson, 2008; Santangelo, 2006; Sanz et al., 2016). This forces cells to switch into the third state, termed the ''diauxic shift,'' where cellular processes are remodeled to prepare for further proliferation in the fourth ''post-diauxic growth phase.'' Here, growth is dependent on respiratory metabolism of non-fermentable carbon sources, including the consumption of ethanol and requires remodeling of mitochondria (Di Bartolomeo et al., 2020). Finally, cells enter the fifth quiescent ''stationary phase,'' where proliferation ceases due to exhaustion of a nutrient (Pedruzzi et al., 2000). Counterintuitively, quiescent cells are metabolically active, remain viable for up to 25 days (Pedruzzi et al., 2000) and can swiftly reenter the life cycle when provided with new nutrients. A critical signaling component during quiescence is the Greatwall/MASTL kinase ortholog Rim15 (Swinnen et al., 2006), which is attenuated during exponential growth by phosphorylation via the PKA, TORC1, and PHO pathways (Pedruzzi et al., 2003; Wanke et al., 2005), highlighting the specificity and interconnectedness of physiological and biochemical traits within each stage of the yeast life cycle.

Using time-resolved lipidomics and proteomics analysis, we have previously uncovered that the yeast life cycle is also accompanied by extensive lipid metabolic remodeling (Casanovas et al., 2015). In particular, the lag and exponential phases are characterized by mobilization of storage lipids, increased levels of membrane lipids with saturated and mono-unsaturated FA chains having 10–16 carbon atoms, and modulation of sphingolipid levels. Some evidence suggests that this remodeling involves Cdc28-mediated phosphorylation and activation of the triacylglycerol (TAG) lipase Tgl4 to facilitate the mobilization of storage lipids (Kurat et al., 2009), PKA-mediated activation of the choline kinase Cki1 to direct flux toward membrane lipid biosynthesis via the Kennedy pathway (Yu et al., 2002), and TORC2-mediated activation of sphingolipid biosynthesis (Breslow et al., 2010; Muir et al., 2014; Roelants et al., 2011). Interestingly, the lipidome of later stages also features extensive remodeling, which so far has only been ascribed to changes in enzyme expression, and it is currently unknown whether specific signaling pathways are important to control lipid metabolic activities during these stages of the yeast life cycle.

Here, we have used quantitative phosphoproteomics to analyze to which extent phosphorylation-based signaling pathways impinge on the dynamics of the lipid metabolic network across the yeast life cycle. Strikingly, we found that 34% of all key lipid metabolic proteins are differentially phosphorylated and identified functional phosphosites (p-sites) in a subset of these using in-depth lipidomics flux analysis of cells with genomically engineered phosphomimetic or phosphodeficient mutations. Furthermore, we uncovered a mechanism for regulation of FA chain length by phosphorylation of the fatty acid synthase (FAS) complex. Our work provides a phosphoproteomics resource for the community and deepens our systems-level understanding of how signaling pathways coordinate the regulation of lipid metabolism and homeostasis.

## RESULTS

### Quantitative Phosphoproteomics Analysis of the Yeast Life Cycle

To study how protein phosphorylation impinges on physiological adaptations, we performed a quantitative phosphoproteomics analysis covering the four main stages of the yeast life cycle: the exponential growth phase (6 h after growth resumption), the diauxic shift (12 h), the post-diauxic growth phase (20 h), and the stationary phase (48 h) (Figures 1A and 1B). Notably, the complete life cycle is only attainable when culturing *S. cerevisiae* in rich media such as YPD and not in standard synthetic defined media (Gray et al., 2004; Hanscho et al., 2012). Overall, our analysis captured the temporal profiles of 14,339 phosphopeptides (p-peptides) ascribed to 2,216 distinct phosphoproteins, having a false discovery rate <1% and a p-site localization confidence >75% (Figure 1C; Table S1). In addition, the analysis also captured the temporal profiles of 4,261 proteins (Table S2). The majority of the identified p-peptides (77%) feature a single p-site (Figure 1D) and have a phosphorylation situated primarily on serine (S) (78%) and to a lesser extent on a threonine (T) (19%) or tyrosine (Y) residue (3%) (Figure 1E). Overall, the obtained results and data metrics are congruent with previously published phosphoproteomics (Hu et al., 2019; Oliveira et al., 2015; Paulo and Gygi, 2015) and proteomics data (Figure S1) (Casanovas et al., 2015). Furthermore, by stringent statistical filtering, we found that the abundance of 7,922 p-peptides (55%) belonging to 1,792 phosphoproteins is significantly changed ($q$-value < 0.01) by >2-fold at least at one time point relative to the exponential phase (6 h) (Figure 1C).

To explore the extent to which regulated phosphorylation events occur throughout the life cycle, we clustered the regulated p-peptides by their time of maximum abundance. This revealed an uneven distribution of phosphorylation activity with 42% (3284) and 32% (2512) of regulated p-peptides being most abundant during the exponential phase (6 h) and stationary phase (48 h), respectively (Figure 2A). In comparison, 16% (1295) and 10% (831) of the regulated p-peptides were most abundant during the diauxic shift (12 h) and post-diauxic growth phase (20 h), respectively. Additional analysis showed that this uneven distribution of phosphorylation events is also prominent for both protein kinases and phosphatases (Figure 2B), as well as components of the lipid metabolic network (Figure 2C). As such, our data demonstrate that regulated phosphorylation events occur across all stages of the yeast life cycle and impinge on components of signaling pathways and the lipid metabolic network.

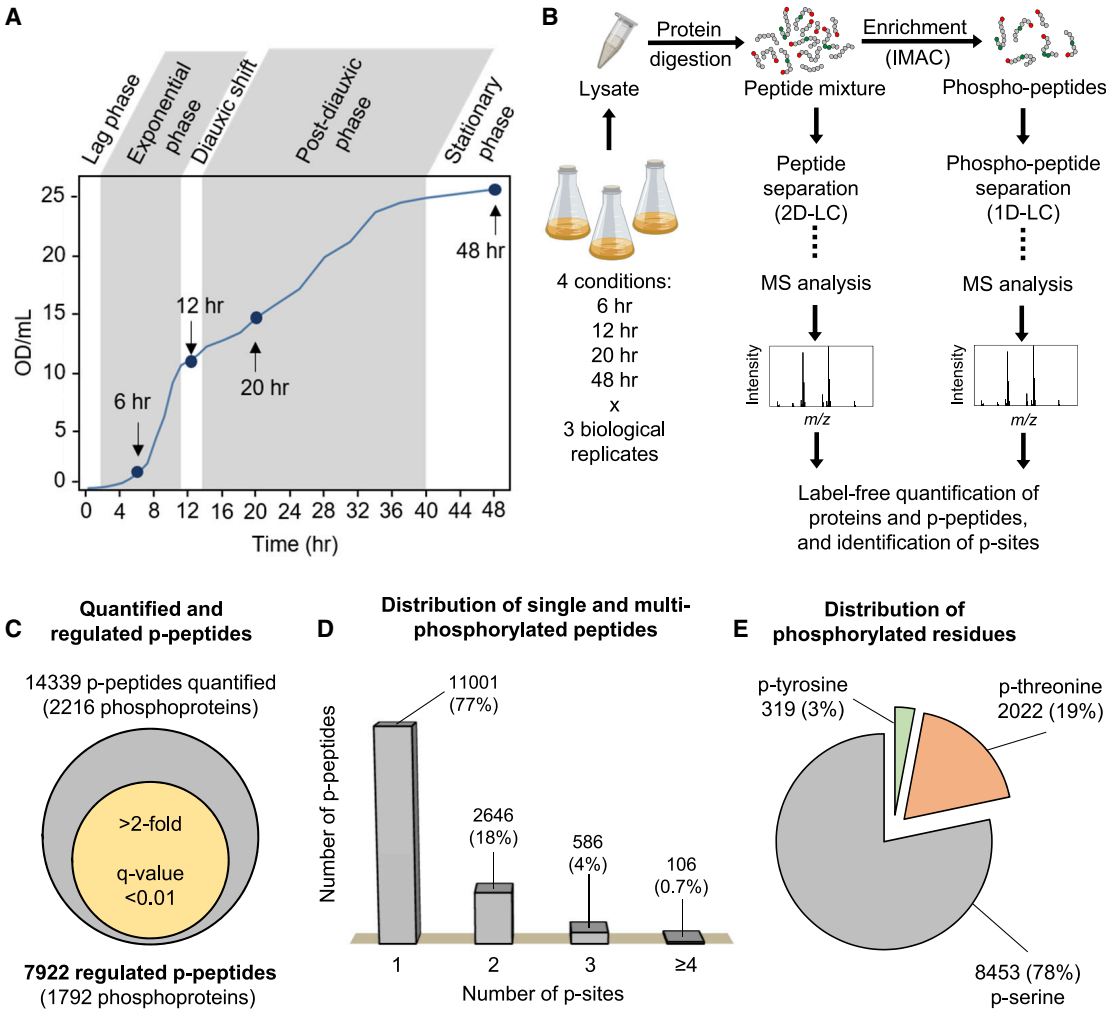


**Figure 1. Quantitative Phosphoproteomics Analysis across the Life Cycle of *S. cerevisiae***

(A) Growth curve of *S. cerevisiae* showing the main stages of the yeast life cycle at the top. Shaded areas correspond to phases of cell proliferation. Time points for phosphoproteomics analysis are indicated with blue circles.

(B) Outline of the phosphoproteomics analysis. Samples were processed for both quantitative label-free proteomics by 2D liquid chromatography-tandem mass spectrometry (LC-MS/MS) analysis and quantitative phosphoproteomics using immobilized metal affinity chromatography (IMAC)-based isolation of p-peptides followed by 1D LC-MS/MS analysis.

(C) Number of quantified and regulated p-peptides and phosphoproteins. Regulated p-peptides change >2-fold and have a $q$-value < 0.01 at least at one time point versus the 6-h time point.

(D) Number of monitored p-peptides containing one, two, three, or more than three p-sites.

(E) Number of phosphorylated serine, threonine, and tyrosine residues in the identified p-peptides.

See also Figure S1.

## Growth-Phase-Specific Signaling Signatures Are Mediated by Nutrient-Sensing Pathways

Next, we assessed whether the growth-phase-specific phosphorylation events are linked to activities of distinct signaling pathways. To do so, we carried out motif enrichment and kinase prediction analyses using the algorithms MoMo and NetworKIN, respectively (Cheng et al., 2018; Horn et al., 2014). This revealed that each stage of the life cycle is characterized by both unique and common p-site motifs that can be attributed to activities of various kinases and kinase groups (Figures 2D, S2A, and S2B). During the exponential growth phase, we found a particular enrichment in the p-site motifs S/T-P, S/T-P-x-K, and S/T-P-x-x-K, which indicate increased activity of the CMGC kinases Cdc28, Slt2, Pho85, Fus3, and Kss1, all of which have a role in cell-cycle regulation. Furthermore, we found the PKA-like consensus motifs R-x-x-S/T, R-R-x-S/T, and R-S-x-S/T (Kennelly and Krebs, 1991; Shabb, 2001) enriched suggesting high activity of Tpk1 kinase (Figure 2D).

Among the diauxic-shift-specific phosphorylation events, we found the AMPK-like consensus motifs S/T-x-x-x-L, R-x-x-S/T, and K-x-x-S/T (Hardie et al., 2016) to be enriched highlighting the Snf1 kinase as a key mediator of the physiological

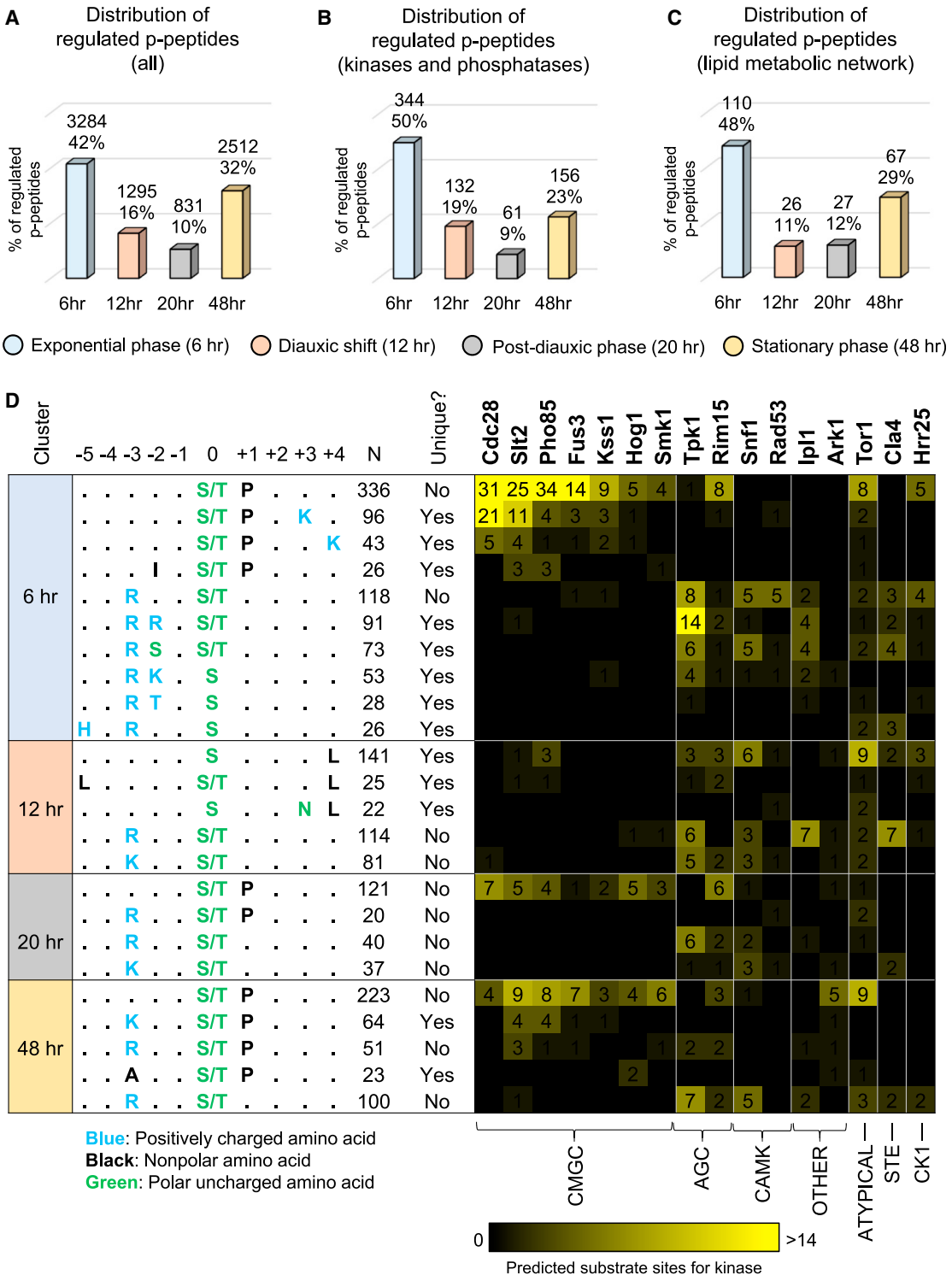


**Figure 2. Remodeling of the Yeast Phosphoproteome during Growth Adaptations**

(A) Proportion of regulated p-peptides with maximum abundance at the time points 6, 12, 20, and 48 h.

(B) Proportion of regulated p-peptides from protein kinases and phosphatases with maximum abundance at the indicated time points.

(C) Proportion of regulated p-peptides from lipid metabolic machinery with maximum abundance at the indicated time points.

(D) Enrichment analysis of p-site motifs and kinase prediction for regulated p-peptides. Motifs enriched in p-peptides having maximum abundance at 6, 12, 20, or 48 h (left panel). The column "N" reports the number of p-peptide sequences matching a given motif, and the column "Unique" specifies whether the motif is

*(legend continued on next page)*

adaptation from fermentative to respiratory metabolism. We also found that the majority of Snf1 p-sites, including two previously unknown p-sites at S256 and S391, are at their highest level during the diauxic shift, which further supports its importance during this growth stage (Figure S2C). Moreover, also phosphorylation of Elm1, a Snf1-activating kinase (Sutherland et al., 2003), at S581 is at its highest level during the diauxic shift (Figure S2D).

The specific phosphorylation events in the post-diauxic growth phase (20 h) and stationary phase (48 h) showed the common S/T-P motif to be most enriched and surprisingly ascribed to primarily Cdc28 and Rim15-mediated signaling (Figure 2D). This suggests that Cdc28 also participates in cell proliferation when growth is powered by respiratory metabolism and that Rim15 is activated after the diauxic shift in order to turn on cellular processes that support entry and survival in the quiescence stationary phase (Luo et al., 2011). Notably, this final growth stage featured the three distinct p-site motifs K-x-x-S/T-P, A-x-x-S/T-P, and R-x-x-S/T-P, where the latter is exclusively shared with the post-diauxic growth phase. Interestingly, these unique motifs are, in contrast to most other identified p-site motifs, less frequently associated with the activity of a kinase, probably because kinases that are important for entry into the quiescence state are underrepresented in databases of curated consensus motifs.

Taken together, our quantitative phosphoproteomics resource recapitulates hallmarks of key signaling pathways that control cell proliferation during the exponential phase (e.g., Cdc28 and PKA) and adaptation in the diauxic shift (i.e., Snf1). Furthermore, our resource provides insights into phosphorylation events that are specific for cell proliferation and establishment of quiescence in the less well-characterized post-diauxic growth phase and stationary phase.

## Differential Phosphorylation Mediates Reprogramming of the Lipid Metabolic Network

Given the coupling between signaling pathways and regulation of lipid metabolism, we next evaluated how constituents of the lipid metabolic network are differentially phosphorylated across the life cycle. Out of 146 lipid metabolic enzymes and regulators, we found 63 (43%) to be phosphorylated (Figure 3A) and together account for 285 distinct p-sites. Notably, 50 of these phosphoproteins showed significant changes in their phosphorylation state, demonstrating that at least 34% of the lipid metabolic machinery is subject to phosphoregulation (Figure 3B). Fourteen of those proteins displayed both differential expression and phosphorylation across the yeast life cycle.

Inspection of proteins with regulated p-peptides showed that these cover all major lipid metabolic pathways (Figure 3A). Among the lipid enzymes that are the most differentially phosphorylated, we found several with previously reported phosphoregulation, including the acetyl-coenzyme A (acetyl-CoA) carboxylase Acc1 (Woods et al., 1994), the polyphosphatidylinositol phosphatase Inp53 (Guiney et al., 2015), the phosphatidylserine (PS) synthase Cho1 (Kinney and Carman, 1988), the PA phosphatase Pah1 (Carman and Han, 2019; Hassaninasab et al., 2019), and the ethanolamine kinase Eki1 (Kim and Carman, 1999) (Figure 3C). Taken together, these data suggest that the lipid metabolic network is extensively reprogrammed by both phosphorylation-based signaling events and at the level of protein expression (Casanovas et al., 2015).

## Identification of Functional P-Sites in Lipid Metabolic Machinery

Next, we investigated whether identified p-sites on lipid enzymes and regulators have a functional role in regulation of lipid metabolic activity. To this end, we focused on regulated p-sites in the following five lipid metabolic proteins (Figure 4): the phosphatidate cytidylyltransferase Cds1 (S40, S42, and T44), the α-subunit of the FAS complex Fas2 (S1440, S1640, and S1827), the long-chain base kinase Lcb5 (S38, S39, T42, S52, S54, S55, S60, T62, S63, S201, and S202), the PS synthase Cho1 (S4, Y32, S34, S46, S47, T53, and T54), and the regulator of sphingolipid synthesis Orm2 (T5, S9, S15, and T18). The reasons for this choice were that phosphoregulation of Cds1 and Fas2, both encoded by essential genes, has not been studied before; the viable deletion strains *lcb5*Δ, *cho1*Δ, and *orm2*Δ display a growth defect on non-fermentable carbon sources (Figure S3A), suggesting that these proteins are important for metabolic homeostasis after the diauxic shift; and these proteins have p-sites at either their N or C termini, which allows easy production of phosphomimetic and phosphodeficient mutants by a single genomic transformation using custom-designed DNA fragments (Figure 4A). By this multiple-site-directed mutagenesis approach, we systematically mutated p-sites in the five candidate proteins to either phosphomimetic glutamate (E) or phosphodeficient alanine (A) residues. Overall, we obtained 11 strains having from 3 to 9 p-site mutations ($cds1^{3A}$, $cho1^{7A}$, $cho1^{7E}$, $fas2^{3A}$, $fas2^{3E}$, $lcb5^{2A}$, $lcb5^{2E}$, $lcb5^{4E}$, $lcb5^{9A}$, $orm2^{4A}$, and $orm2^{4E}$; Figure 4). Notably, two of the mutated p-sites in Cho1 (i.e., S46 and S47) have previously been shown to be functional and mediated by PKA (Choi et al., 2010), and three of the p-sites in Orm2 (i.e., S9, S15, and T18) have been suggested to be involved in the regulation of sphingolipid synthesis by reduced TORC1-mediated inhibition of the kinase Npr1 upon acute nutrient limitation (Shimobayashi et al., 2013). Furthermore, phylogenetic analysis shows that the majority of the mutated p-sites are conserved among most species in the *Saccharomyces* genus and specifically that the p-sites S46 and S47 in Cho1, as well as S1440, S1640, and S1827 in Fas2, are conserved across most of the *Saccharomycetaceae* family of yeast (Table S4). Next, we examined the physiological impact of the mutations by monitoring growth across 48 h in liquid media (Figures 4B–4F). The most severe phenotype was detected for the strain with phosphomimetic mutations in the FAS complex ($fas2^{3E}$). Here, we found an extended lag phase, reduced growth

exclusively found in one of the clusters or not. Predictions of kinases responsible for phosphorylating p-peptides belonging to a given motif (right panel). Only kinases with five or more predictions for at least one motif are shown. The predicted kinases are ascribed to the kinase families indicated at the bottom of the panel.
See also Figure S2.

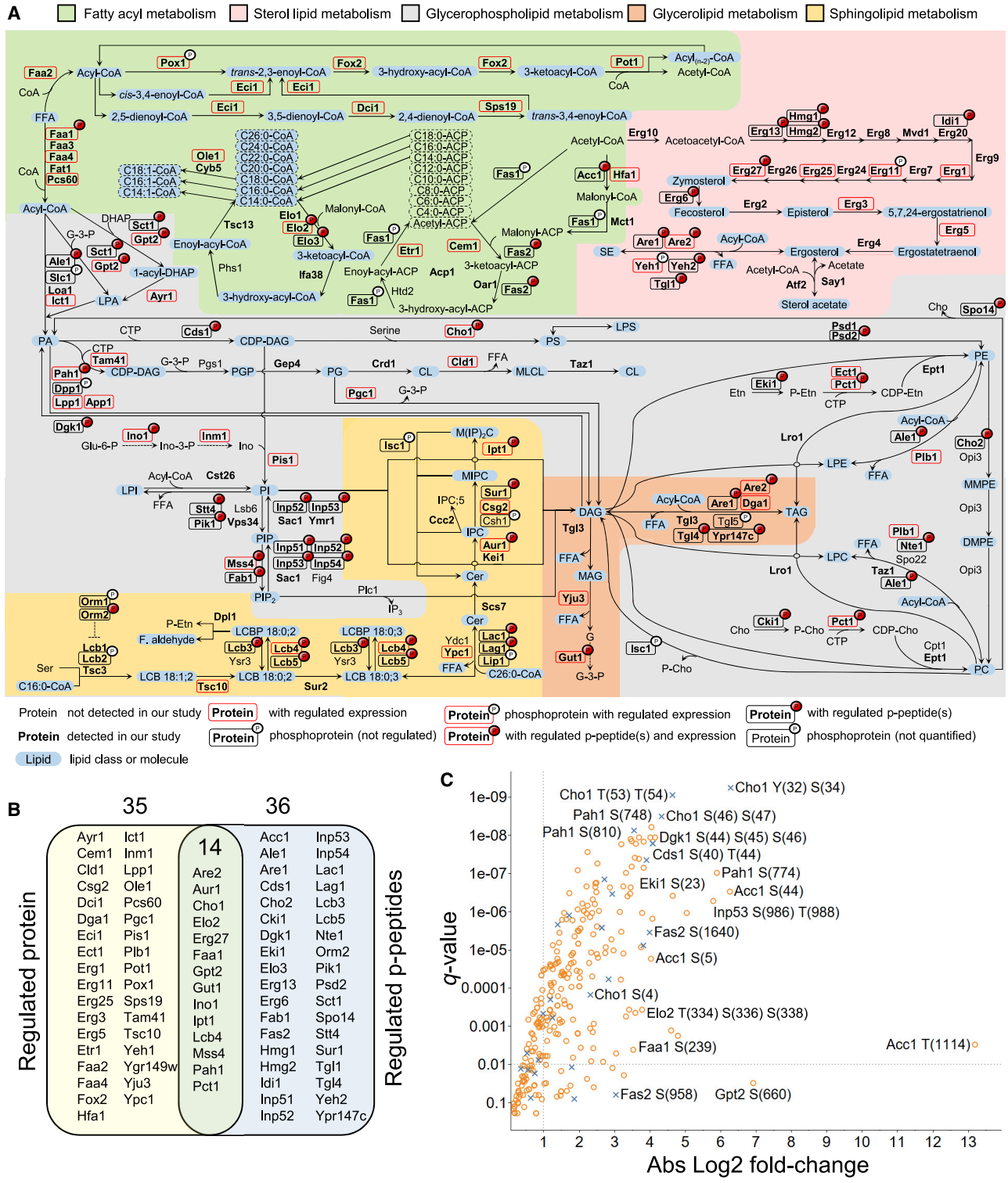


**Figure 3. Phosphorylation-Based Regulation of the Lipid Metabolic Network**

(A) Changes in protein phosphorylation and abundance across the yeast lipid metabolic network. The network was adapted from Casanovas et al. (2015).

(B) Venn diagram of lipid metabolic machinery that are differentially phosphorylated and/or expressed across the yeast life cycle.

(C) Overview of most significant differences in phosphorylation of lipid metabolic proteins. Proteins selected for mutagenesis of p-sites are highlighted with blue crosses (see Figure 4 and related text).

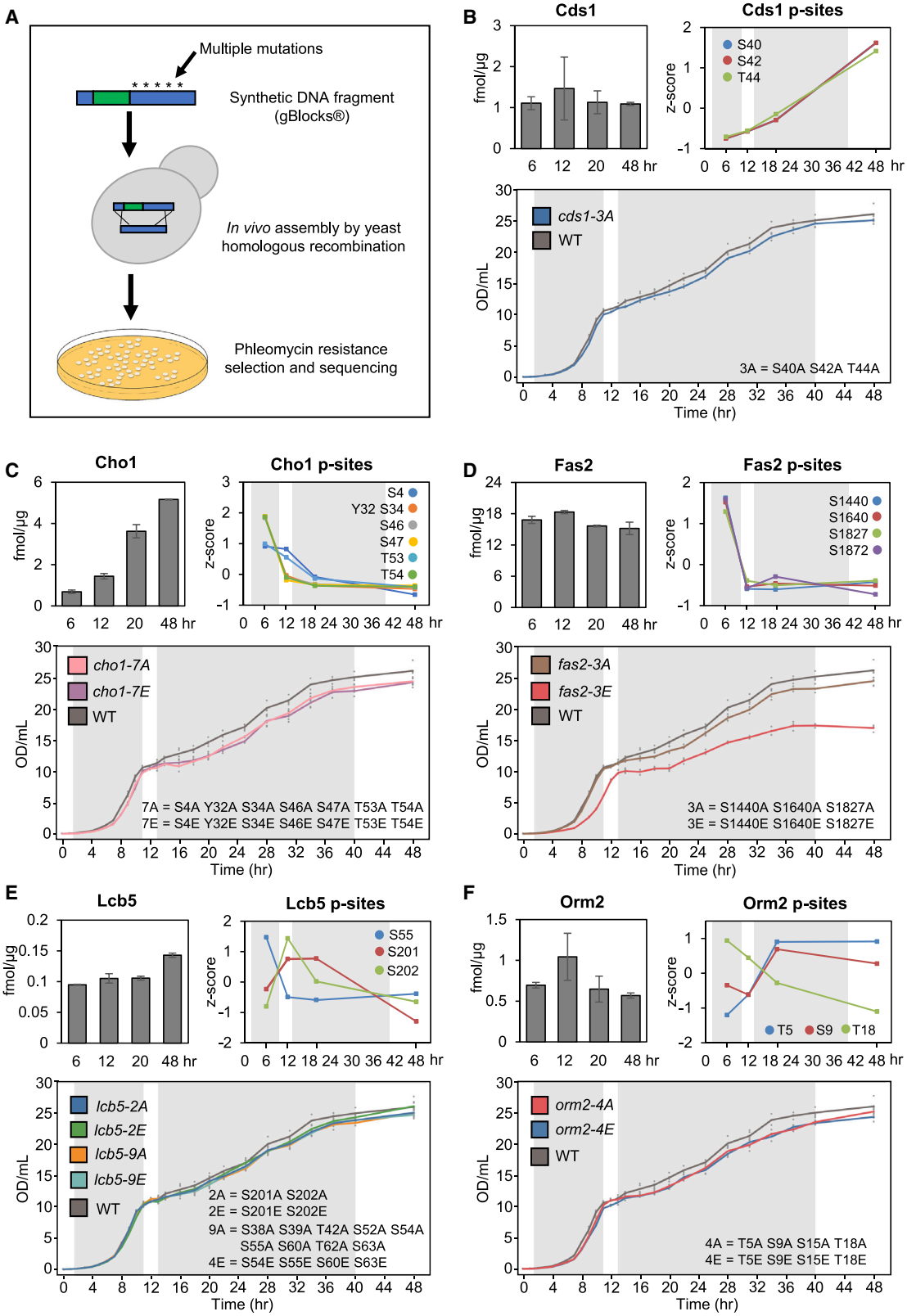


*(legend on next page)*

rate in the exponential phase, and attenuated growth after the diauxic shift. Furthermore, we also noted subtle growth phenotypes for the *cho1*$^{7A}$ and *cho1*$^{7E}$ strains primarily with attenuated growth after the diauxic shift. Surprisingly, none of the other strains displayed a pronounced growth phenotype in either liquid medium or solid medium with glucose and non-fermentable carbon sources (Figure S3B).

## In-Depth Phenotyping by Lipid Metabolic Flux Analysis

For more detailed phenotyping of our mutant strains and to determine whether the identified p-sites are truly functional in regulating lipid metabolic activity, we employed a lipidomics flux assay (Figure 5A) where cells are fed a cocktail of stable isotope-labeled tracers ($^{13}C_3{}^{15}N$-serine, $^{2}H_3$-methionine, $^{2}H_{13}$-choline, and $^{2}H_6$-inositol) and the absolute levels of labeled and unlabeled lipid molecules are quantified simultaneously using high-resolution shotgun lipidomics (Almeida et al., 2015; Ejsing et al., 2009). Importantly, this approach allows system-wide monitoring of biosynthetic activities across the cytidine diphosphate diacylglycerol (CDP-DAG) pathway producing PS, phosphatidylethanolamine (PE), and phosphatidylinositol (PI) lipids, the PE methylation and Kennedy pathways producing phosphatidylcholine (PC) lipids, as well as the sphingolipid and sterol lipid pathways. Using this approach, we examined the lipid metabolic state of wild type and our 11 mutant strains when cultured in either glucose-rich YPD medium or glycerol-rich YPG medium, which served as proxies for cells in the fermentative exponential phase and respiratory post-diauxic growth phase, respectively.

Overall, our lipidomics flux analysis afforded the quantitative monitoring of 390 lipid molecules, whereof 139 were detected as both labeled and unlabeled (Figure S4A; Table S3). Principal-component analysis revealed that the most pronounced lipid metabolic differences during fermentative growth in glucose-rich medium were found in the strains *fas2*$^{3E}$, *cds1*$^{3A}$, *cho1*$^{7A}$, and *cho1*$^{7E}$ (Figures 5B and S4B) (described in further detail below) and that the most pronounced lipid metabolic differences during respiratory growth conditions in glycerol-rich medium were found in the strains *cho1*$^{7E}$ and *fas2*$^{3E}$ (Figures 5C and S4C). Similar to the results obtained by phenotypic assessment by growth, we found that mutations in Lcb5 and Orm2 did not prompt a pronounced lipid metabolic phenotype. This lack of a lipid metabolic phenotype in these strains could be due to the presence of the functionally redundant paralogs Lcb4 and Orm1.

## Lipidomics Flux Analysis Reveals Increased Synthesis of $C_{18}$-Containing Lipids in *fas2*$^{3E}$

The lipidomics flux data for cells carrying the phosphomimetic mutations in the FAS complex (*fas2*$^{3E}$) revealed an unexpected impact on the FA chain length of newly synthesized lipids. In particular, the biosynthesis of $C_{18}$-containing PS, PE, PC, and PI lipids via the CDP-DAG, PE methylation, and Kennedy pathways was increased when *fas2*$^{3E}$ cells were cultured in YPD medium (Figure 5D). At the same time, biosynthesis of lipids having FA chains with 12–16 carbon atoms were markedly reduced. Moreover, the increased level of $C_{18}$-containing lipids was also evident at the steady-state level (Figures 5D and S5A). Interestingly, we found that this lipid metabolic phenotype was less prominent when *fas2*$^{3E}$ cells were cultured under respiratory conditions in YPG medium (Figures 5C and S5B) and specifically that the elevated level of $C_{18}$-containing lipids compared to wild type is less pronounced (Figure S5A). The reason for this latter discrepancy is currently unclear but could be related to a general increase in the production of $C_{18}$-containing lipids during respiratory growth (Figure S5A). Given that Fas2 is a component of the FAS complex, these results suggest that the phosphorylation at S1440, S1640, and/or S1827 could be linked to increased biosynthesis of FA 18:1 and that this FA chain is used for production of membrane lipids during exponential growth under glucose-rich conditions, a mode of regulation that has so far not been described.

## Phosphorylation of Cds1 and Cho1 Increases Enzymatic Activity

The lipid metabolic perturbations in *cds1*$^{3A}$ cells were also primarily observed during exponential growth in YPD. At the lipid-flux level, we observed an overall reduction in PI synthesis and an increase in PC production via the Kennedy pathway, followed by a less pronounced increase in the synthesis of PS and PE (Figure 5E). At the steady-state level, we found increases in total PA, diacylglycerol (DAG), TAG, and PC levels and a reduction in the PI level. In addition, the steady-state level of CDP-DAG, the direct product of Cds1, was 4.2-fold reduced (p value = 0.002) as compared to wild-type cells. Together, these data suggest

**Figure 4. Assessment of Physiological Impact of Multiple P-Site Mutations of Lipid Metabolic Machinery**

(A) Multiple site-directed mutagenesis in a single step. Phosphomimetic or phosphodeficient mutations in candidate proteins are introduced simultaneously by homologous recombination of custom-designed DNA fragments.

(B) Cds1 expression level (upper left) and regulated p-sites (upper right) across the yeast life cycle, and growth characteristics of the mutant *cds1*$^{3A}$ strain and overview of p-sites that have been mutated (bottom).

(C) Cho1 expression level and regulated p-sites, and growth characteristics of the mutant strains *cho1*$^{7A}$ and *cho1*$^{7E}$ and overview of p-sites that have been mutated.

(D) Fas2 expression level and regulated p-sites, and growth characteristics of the mutant strains *fas2*$^{3A}$ and *fas2*$^{3E}$ and overview of p-sites that have been mutated.

(E) Lcb5 expression level and regulated p-sites; growth of the mutant strains *lcb5*$^{2A}$, *lcb5*$^{2E}$, *lcb5*$^{4E}$, and *lcb5*$^{9A}$; and overview of p-sites that have been mutated. Note that several previously reported p-sites in the vicinity of S55 were also mutated in the *lcb5*$^{4E}$ and *lcb5*$^{9A}$ strains.

(F) Orm2 expression level and regulated p-sites, growth of the mutant strains *orm2*$^{4A}$ and *orm2*$^{4E}$, and overview of p-sites that have been mutated. The previously reported p-site S15 was also mutated.

Protein expression levels, determined by dividing the measured fmol on-column protein amount by the total amount of protein on-column (μg protein), represent mean ± SD of three biological replicates; phosphorylation level is expressed as average p-peptide abundance, corrected for protein expression; and cell density (OD/mL) is expressed as the mean two biological and two technical replicates. See also Figure S3.

CellPress
OPEN ACCESS

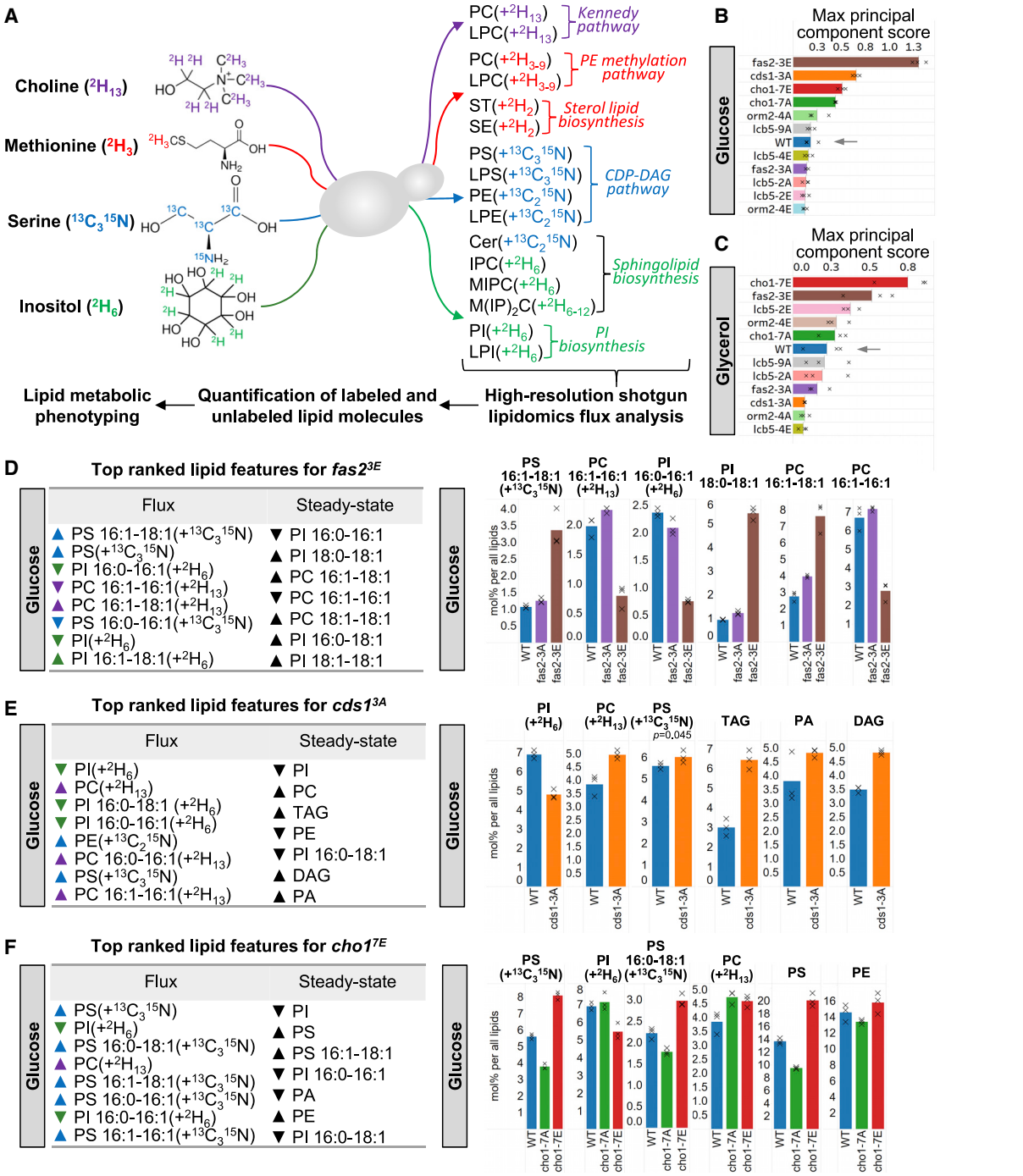


**Figure 5. Phenotyping by Lipidomics Flux Analysis**

(A) Strategy for simultaneous flux analysis across multiple lipid metabolic pathways. Yeast cells cultured in YPD and YPG were fed a cocktail of stable-isotope-labeled serine, inositol, methionine, and choline. Lipid extracts were analyzed by high-resolution shotgun lipidomics for quantification of both labeled (flux) and unlabeled (steady-state levels) lipids. Mutant strains with lipid metabolic phenotypes were identified by principal-component analysis. The metabolic fates of different tracers are highlighted by color-code.

(B) Phenotypic scoring of yeast strains cultured in YPD medium, used as a proxy for fermentative growth during the exponential phase.

(C) Phenotypic scoring of yeast strains cultured in YPG medium, used as a proxy for respiratory growth during the post-diauxic phase.

*(legend continued on next page)*

that the mutant Cds1$^{3A}$ enzyme is less active than the wild-type enzyme, prompting the rerouting of its substrate, PA, to the phosphatase Pah1, which increases DAG production and further promotes its conversion into TAG, as well as PC via the Kennedy pathway. Further, these data also indicate that once CDP-DAG molecules are produced, they become effectively converted to PS instead of PI and subsequently decarboxylated to PE. Notably, this discovery of functional p-sites in Cds1 opens up several new avenues to understand the molecular basis of lipid metabolic pathway cross-talk and the regulation of lipid metabolism under respiratory growth conditions where phosphorylation of Cds1 is increased (Figure 4B).

The lipidomics flux analysis of *cho1*$^{7E}$ cells demonstrated a specific increase in the overall biosynthesis of PS molecules during both fermentative growth in YPD medium (Figure 5F) and respiratory growth in the YPG medium (Figure S5C). Consistently, in cells carrying phosphodeficient residues (*cho1*$^{7A}$), overall PS biosynthesis was reduced, but only under fermentative conditions (Figures 5F and S5C). Together with the initial finding that Cho1 is primarily phosphorylated during the exponential phase (Figure 4C), these data suggest phosphorylation serves to increase PS production during the exponential growth.

## The Fas2$^{3E}$ Protein Prompts Increased 18:0-CoA Synthesis by the FAS Complex

Intrigued by the unexpected lipid metabolic phenotype of *fas2*$^{3E}$ cells, we next investigated how the phosphomimetic mutations lead to the shift of FA chain length and the synthesis of FA-18:1-containing lipid molecules. To this end, we first verified that Fas2$^{3E}$ is expressed at the same level as wild-type Fas2 (Figure S6A).

Next, we aimed at determining which of three theoretically possible metabolic trajectories leads to the increased FA 18:1 production (Figure 6A). Since the product spectrum of the FAS complex is thought to be primarily determined by characteristics of its ketoacyl synthase and malonyl/palmitoyl transferase domains (Gajewski et al., 2017; Johansson et al., 2008), we at first did not consider a major change of its molecular output by direct phosphoregulation but speculated that the association with downstream pathways such as FA elongation and desaturation could be changed. The most likely pathway would therefore involve Elo1- or Elo2-mediated elongation of the canonical FAS product 16:0-CoA to 18:0-CoA (Oh et al., 1997), followed by insertion of a double bond between carbon atoms 9 and 10 to produce oleyl-CoA (i.e., 18:1(9)-CoA) by Ole1, the only FA desaturase in *S. cerevisiae* (Stukey et al., 1990). Alternatively, 16:0-CoA may first be converted to palmitoleyl-CoA (i.e., 16:1(9)-CoA) by Ole1, followed by Elo1- or Elo2-mediated elongation to produce vaccenyl-CoA (i.e., 18:1(11)-CoA). A third possibility could be regulation of FAS itself leading to an increased production of 18:0-CoA, followed by Ole1-mediated synthesis of 18:1(9)-CoA.

To discern between these possibilities, we first determined whether the FAS complex in *fas2*$^{3E}$ cells preferentially produces 16:0-CoA or overproduces 18:0-CoA. To exclude the likely contribution of the elongases, we deleted *ELO1* or *ELO2* in *fas2*$^{3E}$ cells and analyzed their lipidome. To our surprise, this clearly showed that deletion of *ELO1* or *ELO2* does not affect the production of FA 18:1-containing lipids in *fas2*$^{3E}$ cells (Figure S6B), strongly suggesting that the high FA 18:1 level is independent of the endoplasmic reticulum (ER)-embedded elongases Elo1 and Elo2 and is a direct consequence of altered product specificity of the phosphomimetic mutations, leading to increased production of 18:0-CoA and desaturation by Ole1.

To explore this possibility further, we investigated whether elongation of 16:1(9)-CoA to 18:1(11)-CoA occurs. To this end, we performed total FA analysis on *fas2*$^{3E}$ cells (Gallego et al., 2018) and combined this with ozone-induced dissociation (OzID) (Paine et al., 2018) to determine the positions of the double bonds in FA 18:1 chains (Figure 6B). This demonstrated that the signals corresponding to FA 18:1(9) (i.e., oleic acid) are by far the most abundant, representing 94% of the signal intensity in wild type and 98% in *fas2*$^{3E}$. Only 6% and 2% of the signal, respectively, corresponded to FA 18:1(11) (i.e., vaccenic acid) (Figure 6C). Taken together, our results demonstrate that the higher FA 18:1 level in *fas2*$^{3E}$ cells reflects a so-far-unknown direct-phosphorylation-mediated regulation of the product specificity of the FAS complex and does not involve Elo1- or Elo2-mediated elongation of 16:0-CoA or 16:1-CoA.

To further substantiate this finding, we next determined the profile of *de-novo*-synthesized FA chains in wild-type and *fas2*$^{3E}$ cells. To do so, we cultured cells in the presence of $^{13}C_6$-glucose for 90 min, followed by quantifying the total level of newly synthesized $^{13}$C-labeled FA chains. This showed that the *de novo* synthesis of FAs was similar in wild-type and *fas2*$^{3E}$ cells (Figure S6C), suggesting that the *in vivo* activity of the FAS complex in the *fas2*$^{3E}$ is similar to wild-type cells. Furthermore, we indeed found that *fas2*$^{3E}$ cells produce higher levels of FA 18:1 and FA 18:0 than wild-type cells (Figure 6D), showing a 2.6-fold increase of $C_{18}$- over $C_{16}$-containing FA chains (Figure 6E). Notably, we could rule out that the increased production of $C_{18}$-containing FAs is due to defective conversion to very long-chain FAs, since *fas2*$^{3E}$ cells also harbored a higher level $^{13}$C-labeled FA 26:0 (Figure 6D).

Furthermore, to directly test whether the FAS complex in *fas2*$^{3E}$ cells produces a higher proportion of 18:0-CoA, we next carried out an *in vitro* assay to profile the FAS product specificity. To this end, we prepared cytosolic fractions containing the FAS complex and measured the incorporation of $^{13}C_3$-labeled malonyl-CoA into *de-novo*-synthesized FA chains (Topolska et al., 2020). Consistent with our results *in vivo*, the cytosol of *fas2*$^{3E}$ cells produced a higher proportion of $^{13}$C-labeled FA 18:0 (Figure 6F) and yielded a 1.6-fold increased ratio between $C_{18}$- and $C_{16}$-containing FA chains as compared to wild-type cells

(D–F) Summary of lipid metabolic hallmarks of indicated mutant strains cultured in YPD (left panels) and examples of lipidome differences compared to wild type (right panels). Increased and decreased lipid features are indicated by triangular arrows (▲ and ▼, respectively), which for labeled lipid features are color-coded according to metabolic fates shown in (A). Note that lipid features include both individual lipid molecules and lipid classes.
Data represent mean values and crosses individual measurements (n = 3 biological replicates). Statistical significance was calculated with Student's *t*-test.See also Figures S4 and S5.

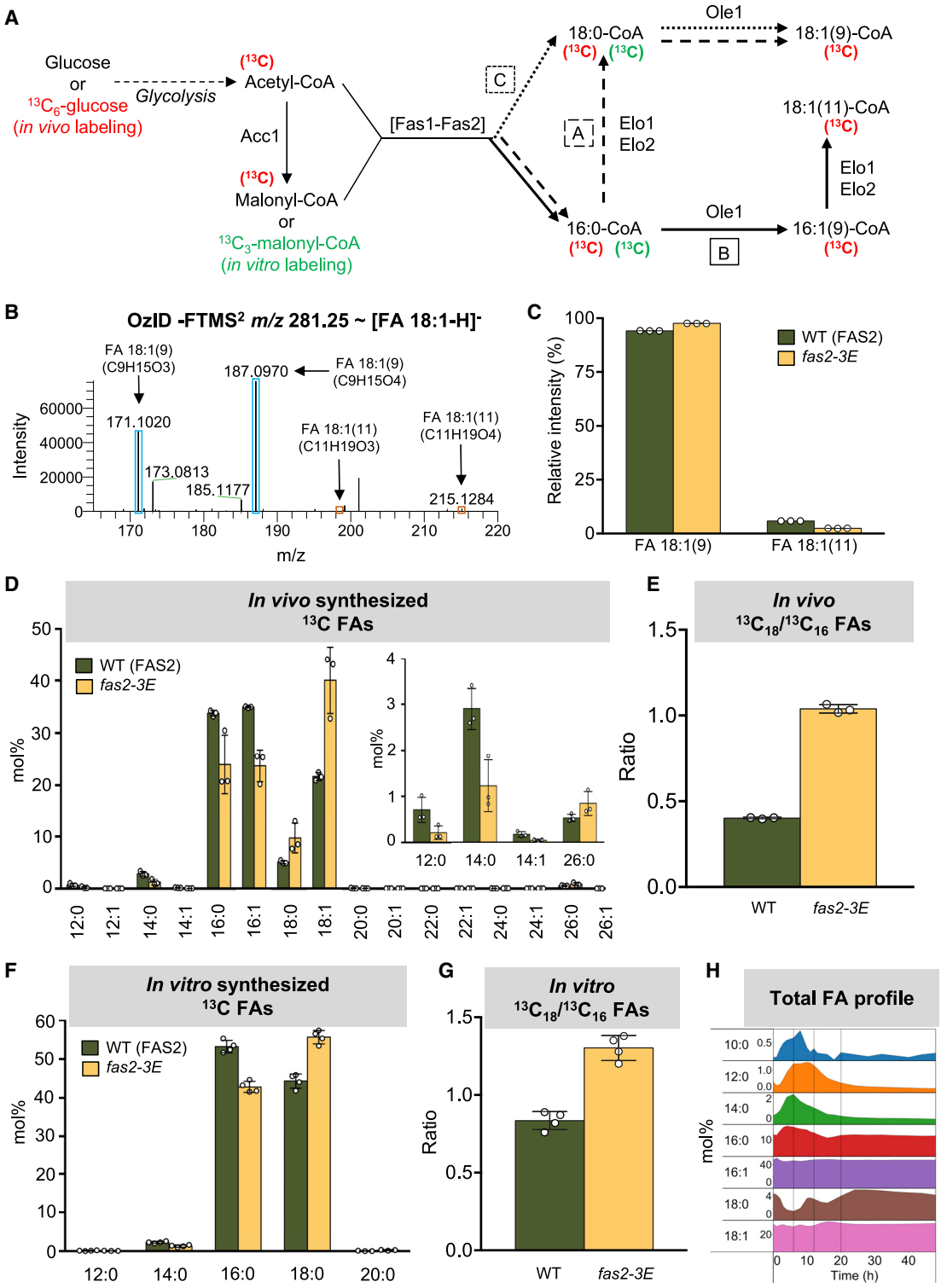


**Figure 6. *fas2*$^{3E}$ Mutant Cells Synthesize FA 18:0 at the Expense of Shorter FA Chains**

(A) Overview of *de novo* FA biosynthesis. Multistep pathways are indicated by dashed lines. Potential molecular fates of synthesized 16:0-CoA and 18:0-CoA are highlighted by pathways A, B, and C (see text for details). Precursors utilized for *in vivo* and *in vitro* labeling, relevant for (D)–(G), are highlighted in red and green, respectively.

(B) OzID-FTMS$^2$ spectrum of FA 18:1 from wild-type cells. Detected double-bond location-specific OzID fragments are annotated and highlighted in blue if derived from oleic acid (i.e., FA 18:1(9)) and in brown if derived from vaccenic acid (i.e., FA 18:1(11)).

*(legend continued on next page)*

(Figure 6G). Importantly, no unsaturated $^{13}$C-labeled FAs were detected, demonstrating that the assay was carried out without interference from ER-embedded Ole1 and the elongases. Moreover, the synthesis of $^{13}$C-labeled FA chains was mediated exclusively by the cytosolic FAS complex, as the FAS inhibitor cerulenin completely abolished the production of $^{13}$C-labeled FA chains in both wild-type and *fas2*$^{3E}$ cells (data not shown). Taken together, these data demonstrate that the higher level of $C_{18}$-containing FA chains in *fas2*$^{3E}$ cells is not due to elongation of 16:0-CoA (Figure 6A, pathways A and B); rather, it is due to altered product specificity of the FAS complex prompting the production of 18:0-CoA, which is subsequently desaturated by Ole1 (Figure 6A, pathway C).

## DISCUSSION

In this study, we characterized the regulatory landscape of protein phosphorylation across the yeast life cycle and investigated its impact on the regulation of lipid metabolism at the systems level. This entailed generating a resource of signaling events covering 14,339 p-sites ascribed to 2,216 phosphoproteins. This resource recapitulates the expected hallmarks of PKA, Cdc28, and AMPK signaling during the exponential growth phase and diauxic shift and shows that signaling events in the less-studied post-diauxic phase and stationary phase are highly prominent and feature unique p-site motifs that are, surprisingly, less likely to be recognized by available kinase prediction algorithms. Specifically, we investigated phosphorylation-based regulation of lipid metabolism revealing functional p-sites in key lipid metabolic proteins. These insights were achieved using a strategy where multiple p-sites are mutated simultaneously into phosphomimetic or phosphodeficient alleles and mutant strains are phenotyped by lipidomics flux analysis covering all major lipid metabolic pathways. Finally, we carried out an in-depth characterization of the mutant Fas2$^{3E}$ protein, with which we discovered that the product specificity of the FAS complex can be regulated by phosphorylation.

In addition to providing a resource that can be used to explore how a wide array of cellular processes are governed by signaling pathways under different physiological states, we also shortlist 50 components of the lipid metabolic network that are potentially regulated by signaling events and can be the subject of future investigations. For such investigations we documented the efficacy of a top-down approach where multiple p-sites in candidate proteins are simultaneously mutated by genome editing using custom-designed DNA fragments followed by examining the physiological and metabolic impact of all p-sites collectively in a single mutant strain. This contrasts the traditional bottom-up approach where distinct p-sites are mutated individually using plasmid-based vectors and generates a multitude of mutants that often have no discernible phenotype (Studer et al., 2016). Using our top-down approach helped uncover that phosphorylation at one or several of the p-sites S40, S42, and/or T44 in the phosphatidate cytidylyltransferaseCds1 increases its activity and that this phosphorylation is progressively upregulated from the diauxic shift to the stationary phase. We speculate that this could serve to more effectively shunt the biosynthetic intermediate PA, via CDP-DAG, into PS and PI to maintain their levels during these nutrient-limited stages. The three p-sites are evolutionary conserved in the genus *Saccharomyces* and have no predicted kinase recognizing them, albeit a neighboring proline residue makes the motif of T44 (i.e., SESVTPVTK) a potential consensus site for a CMGC kinase. The lower degree of phosphorylation does not preclude biosynthetic flux through the Cds1-catalyzed pathway during exponential growth, where production of PS, PE, and PI lipids are required for membrane expansion. Corroborating this, we also show that phosphorylation at several p-sites in the downstream PS synthase Cho1 are specifically increased during the exponential phase and that this increases its activity. The two conserved sites, S46 and S47, have previously been shown to be mediated by PKA signaling during exponential growth and modulate activity (Choi et al., 2010), whereas the third and less conserved site, T53, is comprised in a motif predicted to be phosphorylated by Rim15 (i.e., FSINTTPLA). We did not find any predicted kinases for the other four regulated p-sites in Cho1. Notably, more work is needed to ascertain not only the regulatory impact of the individual p-sites in both Cds1 and Cho1 but also which kinases and phosphatases mediate their phosphoregulation.

We selected the Fas2$^{3E}$ protein for in-depth characterization and found evidence for control of FA chain length by phosphoregulation of the FAS complex. Our initial phenotyping revealed that mutating the three p-sites (S1440, S1640, and S1827) in Fas2 into phosphomimetic residues (i.e., Fas2$^{3E}$), but not into phosphodeficient residues (i.e., Fas2$^{3A}$), increases the biosynthesis of $C_{18}$-containing lipids during fermentative growth in YPD medium and that this is less pronounced during respiratory growth in YPG medium. Further analysis uncovered that the phosphorylation prompts the FAS complex to produce higher levels of 18:0-CoA instead of primarily the canonical 16:0-CoA. This finding triggers a range of physiological as well as mechanistic questions about the underpinnings of this significant change in the FAS product landscape.

To gain insight into the physiological context for the control of FA chain length, we carried out an *in silico* total FA analysis of our recently reported lipidomics resource of the yeast life cycle (Figure 6H) (Casanovas et al., 2015). This revealed that the level of FA 18:0 chains in the lipidome is severely reduced only during the exponential growth phase and relatively constant throughout all other stages. Moreover, the analysis also revealed that FA

(C) Abundance of FA 18:1(9) (oleic acid) and FA 18:1(11) (vaccenic acid) in wild-type and *fas2*$^{3E}$.
(D) Profile of $^{13}$C-labeled FAs made *in vivo* by wild-type and *fas2*$^{3E}$ cells using $^{13}C_6$-glucose.
(E) Ratio between $^{13}$C-labeled $C_{18}$- and $C_{16}$-containing FA chains produced *in vivo* by wild-type and *fas2*$^{3E}$ cells.
(F) Profile of $^{13}$C-labeled FAs made *in vitro* by incubating cytosolic fractions from wild-type and *fas2*$^{3E}$ with $^{13}C_3$-malonyl-CoA.
(G) Ratio between $^{13}$C-labled $C_{18}$- and $C_{16}$-containing FA chains produced *in vitro* by cytosolic fractions from wild-type and *fas2*$^{3E}$ cells.
(H) Distribution of FA chains across the yeast life cycle. Data were generated by reanalyzing resource data (Casanovas et al., 2015).
Data represent mean ± SD of at least three biological replicates. See also Figure S6.

18:1 chains are maintained at a relatively constant level. This suggests that phosphorylation of the FAS complex could serve to mitigate the very low FA 18:0 level during exponential growth and thereby increase the production of 18:0-CoA, which is then swiftly siphoned off for 18:1(9)-CoA production by the desaturase Ole1 and incorporation into membrane lipids to maintain membrane homeostasis (Covino et al., 2016). Alternatively, the 18:0-CoA could be used for stearoylation of specific membrane proteins to counteract mitochondrial dysfunction, as has recently been shown in mammalian cells (Senyilmaz et al., 2015).

Insights into the molecular mechanism by which phosphorylation of FAS increases the production of 18:0-CoA is part of future work. Several mechanistic aspects will be explored. These include examining whether phosphorylation perturbs the structure of the FAS complex or its interaction with other proteins. At the structural level, we speculate that a structural change in the reaction chamber leads to an additional turn of the elongation cycle and thereby increased production of 18:0-CoA (Gipson et al., 2010), akin to the caliper mechanism of the ER-embedded FA elongases (Denic and Weissman, 2007). However, the higher synthesis of 18:0-CoA could also be attributed to altered kinetics of FA-CoAs unloading via the Fas1-situated malonyl/palmitoyl transferase domain, which is in proximity to the identified p-sites of Fas2 (Johansson et al., 2009). Mapping the p-sites S1440 and S1827 on the structure of the FAS complex shows that they are positioned at the periphery of the central wheel, outside the reaction chamber, whereas S1640 is inside a cavity juxtapositioned by apolar amino acids (Figure S6D), which is possibly less accessible for a kinase in this conformation. Interestingly, recent cryoelectron microscopy data show additional density at S1440, suggesting that this residue is indeed phosphorylated *in vivo* (Joppe et al., 2020). Moreover, the protein sequence surrounding the p-site S1440 (i.e., VKYASPNLN) is an S-P consensus motif for Cdc28 and related CMGC kinases, that of S1640 (i.e., VRAVSITSF) is an R-x-x-S consensus motif for PKA and related AGC kinases, and that of S1827 (LGVKSLGGG) does not resemble any hitherto-known kinase consensus motif. More work is clearly needed to determine whether phosphorylation of one or a combination of the three p-sites is responsible for the modulation of the FAS product landscape, and it will be interesting to identify the responsible kinase(s).

In summary, our study provides a comprehensive resource of protein phosphorylation events across the yeast life cycle, uncovers that signaling pathways impinge on multiple pathways in the lipid metabolic network, and lays the groundwork for future mechanistic studies into the regulation of the lipid metabolism at the systems level.

## STAR★METHODS

Detailed methods are provided in the online version of this paper and include the following:

- KEY RESOURCES TABLE
- RESOURCE AVAILABILITY
  - Lead Contact
  - Materials Availability
  - Data and Code Availability
- EXPERIMENTAL MODEL AND SUBJECT DETAILS
  - Yeast strains and growth conditions
- METHOD DETAILS
  - Sample preparation for phosphoproteomics analysis of the yeast life cycle
  - Phosphopeptide enrichment
  - LC-MS/MS analysis of (phospho)peptides
  - Peptide identification
  - Spot assay
  - Lipidomics flux analysis
  - Flow cytometry
  - *In vivo* FAS activity and double bond position analysis
  - *In vitro* FAS activity analysis
- QUANTIFICATION AND STATISTICAL ANALYSIS
  - Protein and phosphopeptide quantification
  - Statistical analysis of phosphoproteomics data
  - Bioinformatic analysis of phosphoproteomics data
  - Phylogenetic analysis
  - Lipid abundances from mass spectrometric data

## SUPPLEMENTAL INFORMATION

Supplemental Information can be found online at https://doi.org/10.1016/j.celrep.2020.108024.

## ACKNOWLEDGMENTS

We thank Robin W. Klemm, Alba Diz-Muñoz, Nils J. Færgeman, Florian Fröhlich, and Tushar More for constructive comments and Kristina Egede Budtz and Peter Højrup for amino acid analysis. This research was supported by the Villum Foundation (VKR023439, C.S.E.), the VILLUM Center for Bioanalytical Sciences (VKR023179, O.N.J. and C.S.E.), the Lundbeckfonden (R44-A4342 and R54-A5858, C.S.E.), the Danish Council for Independent Research, Natural Sciences (10-094213, A.C.; 09-072484, C.S.E.), and a Marie Curie Intra-European Fellowship (A.C.). The research leading to these results has received funding from the European Union Seventh Framework Programme (FP7-2007-2013) under grant agreement "HEALTH-F2-2013-602222 (Athero-Flux)" (O.N.J. and C.S.E.).

## AUTHOR CONTRIBUTIONS

A.C., C.S.E., and F.M.-M. conceived and designed the study. A.C., B.L.J.P., D.L.M., F.M.-M., M.T., and R.R.S. conducted the experiments. A.C., C.S.E., F.M.-M., M.M.-T., and R.R.S. analyzed data. A.C., C.S.E., and F.M.-M. wrote the paper. C.S.E., M.H., S.J.B., and O.N.J. supervised the project.

## DECLARATION OF INTERESTS

The authors declare no competing interests.

Received: February 14, 2020
Revised: May 11, 2020
Accepted: July 21, 2020
Published: August 11, 2020

## REFERENCES

Almeida, R., Pauling, J.K., Sokol, E., Hannibal-Bach, H.K., and Ejsing, C.S. (2015). Comprehensive lipidome analysis by shotgun lipidomics on a hybrid quadrupole-orbitrap-linear ion trap mass spectrometer. J. Am. Soc. Mass Spectrom. *26*, 133–148.

Breslow, D.K., Collins, S.R., Bodenmiller, B., Aebersold, R., Simons, K., Shevchenko, A., Ejsing, C.S., and Weissman, J.S. (2010). Orm family proteins mediate sphingolipid homeostasis. Nature *463*, 1048–1053.

Carman, G.M., and Han, G.S. (2019). Fat-regulating phosphatidic acid phosphatase: a review of its roles and regulation in lipid homeostasis. J. Lipid Res. *60*, 2–6.

Casanovas, A., Sprenger, R.R., Tarasov, K., Ruckerbauer, D.E., Hannibal-Bach, H.K., Zanghellini, J., Jensen, O.N., and Ejsing, C.S. (2015). Quantitative analysis of proteome and lipidome dynamics reveals functional regulation of global lipid metabolism. Chem. Biol. *22*, 412–425.

Cheng, A., Grant, C.E., Noble, W.S., and Bailey, T.L. (2018). MoMo: discovery of statistically significant post-translational modification motifs. Bioinformatics *35*, 2774–2782.

Choi, H.S., Han, G.S., and Carman, G.M. (2010). Phosphorylation of yeast phosphatidylserine synthase by protein kinase A: identification of Ser46 and Ser47 as major sites of phosphorylation. J. Biol. Chem. *285*, 11526–11536.

Coller, H.A. (2019). The paradox of metabolism in quiescent stem cells. FEBS Lett. *593*, 2817–2839.

Conrad, M., Schothorst, J., Kankipati, H.N., Van Zeebroeck, G., Rubio-Texeira, M., and Thevelein, J.M. (2014). Nutrient sensing and signaling in the yeast Saccharomyces cerevisiae. FEMS Microbiol. Rev. *38*, 254–299.

Covino, R., Ballweg, S., Stordeur, C., Michaelis, J.B., Puth, K., Wernig, F., Bahrami, A., Ernst, A.M., Hummer, G., and Ernst, R. (2016). A eukaryotic sensor for membrane lipid saturation. Mol. Cell *63*, 49–59.

DeBose-Boyd, R.A., and Ye, J. (2018). SREBPs in lipid metabolism, insulin signaling, and beyond. Trends Biochem. Sci. *43*, 358–368.

Denic, V., and Weissman, J.S. (2007). A molecular caliper mechanism for determining very long-chain fatty acid length. Cell *130*, 663–677.

Di Bartolomeo, F., Malina, C., Campbell, K., Mormino, M., Fuchs, J., Vorontsov, E., Gustafsson, C.M., and Nielsen, J. (2020). Absolute yeast mitochondrial proteome quantification reveals trade-off between biosynthesis and energy generation during diauxic shift. Proc. Natl. Acad. Sci. USA *117*, 7524–7535.

Di Tommaso, P., Moretti, S., Xenarios, I., Orobitg, M., Montanyola, A., Chang, J.M., Taly, J.F., and Notredame, C. (2011). T-Coffee: a web server for the multiple sequence alignment of protein and RNA sequences using structural information and homology extension. Nucleic Acids Res. *39*, W13–W17.

Ejsing, C.S., Sampaio, J.L., Surendranath, V., Duchoslav, E., Ekroos, K., Klemm, R.W., Simons, K., and Shevchenko, A. (2009). Global analysis of the yeast lipidome by quantitative shotgun mass spectrometry. Proc. Natl. Acad. Sci. USA *106*, 2136–2141.

Ellis, S.R., Paine, M.R.L., Eijkel, G.B., Pauling, J.K., Husen, P., Jervelund, M.W., Hermansson, M., Ejsing, C.S., and Heeren, R.M.A. (2018). Automated, parallel mass spectrometry imaging and structural identification of lipids. Nat. Methods *15*, 515–518.

Ernst, R., Ejsing, C.S., and Antonny, B. (2016). Homeoviscous adaptation and the regulation of membrane lipids. J. Mol. Biol. *428* (*24 Pt A*), 4776–4791.

Ewald, J.C. (2018). How yeast coordinates metabolism, growth and division. Curr. Opin. Microbiol. *45*, 1–7.

Futerman, A.H., and Hannun, Y.A. (2004). The complex life of simple sphingolipids. EMBO Rep. *5*, 777–782.

Gajewski, J., Pavlovic, R., Fischer, M., Boles, E., and Grininger, M. (2017). Engineering fungal de novo fatty acid synthesis for short chain fatty acid production. Nat. Commun. *8*, 14650.

Gallego, S.F., Hermansson, M., Liebisch, G., Hodson, L., and Ejsing, C.S. (2018). Total fatty acid analysis of human blood samples in one minute by high-resolution mass spectrometry. Biomolecules *9*, 9.

Gipson, P., Mills, D.J., Wouts, R., Grininger, M., Vonck, J., and Kühlbrandt, W. (2010). Direct structural insight into the substrate-shuttling mechanism of yeast fatty acid synthase by electron cryomicroscopy. Proc. Natl. Acad. Sci. USA *107*, 9164–9169.

González, A., and Hall, M.N. (2017). Nutrient sensing and TOR signaling in yeast and mammals. EMBO J. *36*, 397–408.

Gray, J.V., Petsko, G.A., Johnston, G.C., Ringe, D., Singer, R.A., and Werner-Washburne, M. (2004). "Sleeping beauty": quiescence in Saccharomyces cerevisiae. Microbiol. Mol. Biol. Rev. *68*, 187–206.

Gueldener, U., Heinisch, J., Koehler, G.J., Voss, D., and Hegemann, J.H. (2002). A second set of loxP marker cassettes for Cre-mediated multiple gene knockouts in budding yeast. Nucleic Acids Res. *30*, e23.

Guiney, E.L., Goldman, A.R., Elias, J.E., and Cyert, M.S. (2015). Calcineurin regulates the yeast synaptojanin Inp53/Sjl3 during membrane stress. Mol. Biol. Cell *26*, 769–785.

Hanscho, M., Ruckerbauer, D.E., Chauhan, N., Hofbauer, H.F., Krahulec, S., Nidetzky, B., Kohlwein, S.D., Zanghellini, J., and Natter, K. (2012). Nutritional requirements of the BY series of Saccharomyces cerevisiae strains for optimum growth. FEMS Yeast Res. *12*, 796–808.

Harayama, T., and Riezman, H. (2018). Understanding the diversity of membrane lipid composition. Nat. Rev. Mol. Cell Biol. *19*, 281–296.

Hardie, D.G., Schaffer, B.E., and Brunet, A. (2016). AMPK: an energy-sensing pathway with multiple inputs and outputs. Trends Cell Biol. *26*, 190–201.

Hassaninasab, A., Hsieh, L.S., Su, W.M., Han, G.S., and Carman, G.M. (2019). Yck1 casein kinase I regulates the activity and phosphorylation of Pah1 phosphatidate phosphatase from *Saccharomyces cerevisiae*. J. Biol. Chem. *294*, 18256–18268.

Hedbacker, K., and Carlson, M. (2008). SNF1/AMPK pathways in yeast. Front. Biosci. *13*, 2408–2420.

Henry, S.A., Kohlwein, S.D., and Carman, G.M. (2012). Metabolism and regulation of glycerolipids in the yeast Saccharomyces cerevisiae. Genetics *190*, 317–349.

Højrup, P. (2015). Analysis of peptides and conjugates by amino acid analysis. Methods Mol. Biol. *1348*, 65–76.

Holthuis, J.C., and Menon, A.K. (2014). Lipid landscapes and pipelines in membrane homeostasis. Nature *510*, 48–57.

Horn, H., Schoof, E.M., Kim, J., Robin, X., Miller, M.L., Diella, F., Palma, A., Cesareni, G., Jensen, L.J., and Linding, R. (2014). KinomeXplorer: an integrated platform for kinome biology studies. Nat. Methods *11*, 603–604.

Hu, Z., Raucci, S., Jaquenoud, M., Hatakeyama, R., Stumpe, M., Rohr, R., Reggiori, F., De Virgilio, C., and Dengjel, J. (2019). Multilayered control of protein turnover by TORC1 and Atg1. Cell Rep. *28*, 3486–3496.e3486.

Husen, P., Tarasov, K., Katafiasz, M., Sokol, E., Vogt, J., Baumgart, J., Nitsch, R., Ekroos, K., and Ejsing, C.S. (2013). Analysis of lipid experiments (ALEX): a software framework for analysis of high-resolution shotgun lipidomics data. PLoS ONE *8*, e79736.

Jiménez, J., Ricco, N., Grijota-Martínez, C., Fadó, R., and Clotet, J. (2013). Redundancy or specificity? The role of the CDK Pho85 in cell cycle control. Int. J. Biochem. Mol. Biol. *4*, 140–149.

Johansson, P., Wiltschi, B., Kumari, P., Kessler, B., Vonrhein, C., Vonck, J., Oesterhelt, D., and Grininger, M. (2008). Inhibition of the fungal fatty acid synthase type I multienzyme complex. Proc. Natl. Acad. Sci. USA *105*, 12803–12808.

Johansson, P., Mulinacci, B., Koestler, C., Vollrath, R., Oesterhelt, D., and Grininger, M. (2009). Multimeric options for the auto-activation of the Saccharomyces cerevisiae FAS type I megasynthase. Structure *17*, 1063–1074.

Joppe, M., D'Imprima, E., Salustros, N., Paithankar, K.S., Vonck, J., Grininger, M., and Kühlbrandt, W. (2020). The resolution revolution in cryoEM requires high-quality sample preparation: a rapid pipeline to a high-resolution map of yeast fatty acid synthase. IUCrJ *7*, 220–227.

Käll, L., Canterbury, J.D., Weston, J., Noble, W.S., and MacCoss, M.J. (2007). Semi-supervised learning for peptide identification from shotgun proteomics datasets. Nat. Methods *4*, 923–925.

Kennelly, P.J., and Krebs, E.G. (1991). Consensus sequences as substrate specificity determinants for protein kinases and protein phosphatases. J. Biol. Chem. *266*, 15555–15558.

Kim, K.H., and Carman, G.M. (1999). Phosphorylation and regulation of choline kinase from Saccharomyces cerevisiae by protein kinase A. J. Biol. Chem. *274*, 9531–9538.

Kinney, A.J., and Carman, G.M. (1988). Phosphorylation of yeast phosphatidylserine synthase in vivo and in vitro by cyclic AMP-dependent protein kinase. Proc. Natl. Acad. Sci. USA *85*, 7962–7966.

Kurat, C.F., Wolinski, H., Petschnigg, J., Kaluarachchi, S., Andrews, B., Natter, K., and Kohlwein, S.D. (2009). Cdk1/Cdc28-dependent activation of the major triacylglycerol lipase Tgl4 in yeast links lipolysis to cell-cycle progression. Mol. Cell *33*, 53–63.

León, I.R., Schwämmle, V., Jensen, O.N., and Sprenger, R.R. (2013). Quantitative assessment of in-solution digestion efficiency identifies optimal protocols for unbiased protein analysis. Mol. Cell. Proteomics *12*, 2992–3005.

Lin, S.C., and Hardie, D.G. (2018). AMPK: sensing glucose as well as cellular energy status. Cell Metab. *27*, 299–313.

Locasale, J.W., and Cantley, L.C. (2011). Metabolic flux and the regulation of mammalian cell growth. Cell Metab. *14*, 443–451.

Luo, X., Talarek, N., and De Virgilio, C. (2011). Initiation of the yeast G0 program requires Igo1 and Igo2, which antagonize activation of decapping of specific nutrient-regulated mRNAs. RNA Biol. *8*, 14–17.

Metsalu, T., and Vilo, J. (2015). ClustVis: a web tool for visualizing clustering of multivariate data using Principal Component Analysis and heatmap. Nucleic Acids Res. *43* (*W1*), W566–W570.

Mizunuma, M., Tsubakiyama, R., Ogawa, T., Shitamukai, A., Kobayashi, Y., Inai, T., Kume, K., and Hirata, D. (2013). Ras/cAMP-dependent protein kinase (PKA) regulates multiple aspects of cellular events by phosphorylating the Whi3 cell cycle regulator in budding yeast. J. Biol. Chem. *288*, 10558–10566.

Moreno-Torres, M., Jaquenoud, M., and De Virgilio, C. (2015). TORC1 controls G1-S cell cycle transition in yeast via Mpk1 and the greatwall kinase pathway. Nat. Commun. *6*, 8256.

Muir, A., Ramachandran, S., Roelants, F.M., Timmons, G., and Thorner, J. (2014). TORC2-dependent protein kinase Ypk1 phosphorylates ceramide synthase to stimulate synthesis of complex sphingolipids. eLife *3*, e03779.

Oh, C.S., Toke, D.A., Mandala, S., and Martin, C.E. (1997). ELO2 and ELO3, homologues of the Saccharomyces cerevisiae ELO1 gene, function in fatty acid elongation and are required for sphingolipid formation. J. Biol. Chem. *272*, 17376–17384.

Oliveira, A.P., Ludwig, C., Zampieri, M., Weisser, H., Aebersold, R., and Sauer, U. (2015). Dynamic phosphoproteomics reveals TORC1-dependent regulation of yeast nucleotide and amino acid biosynthesis. Sci. Signal. *8*, rs4.

Paine, M.R.L., Poad, B.L.J., Eijkel, G.B., Marshall, D.L., Blanksby, S.J., Heeren, R.M.A., and Ellis, S.R. (2018). Mass spectrometry imaging with isomeric resolution enabled by ozone-induced dissociation. Angew. Chem. Int. Ed. Engl. *57*, 10530–10534.

Pauling, J.K., Hermansson, M., Hartler, J., Christiansen, K., Gallego, S.F., Peng, B., Ahrends, R., and Ejsing, C.S. (2017). Proposal for a common nomenclature for fragment ions in mass spectra of lipids. PLoS ONE *12*, e0188394.

Paulo, J.A., and Gygi, S.P. (2015). A comprehensive proteomic and phosphoproteomic analysis of yeast deletion mutants of 14-3-3 orthologs and associated effects of rapamycin. Proteomics *15*, 474–486.

Pedruzzi, I., Bürckert, N., Egger, P., and De Virgilio, C. (2000). Saccharomyces cerevisiae Ras/cAMP pathway controls post-diauxic shift element-dependent transcription through the zinc finger protein Gis1. EMBO J. *19*, 2569–2579.

Pedruzzi, I., Dubouloz, F., Cameroni, E., Wanke, V., Roosen, J., Winderickx, J., and De Virgilio, C. (2003). TOR and PKA signaling pathways converge on the protein kinase Rim15 to control entry into G0. Mol. Cell *12*, 1607–1613.

Rinaldi, J., Wu, J., Yang, J., Ralston, C.Y., Sankaran, B., Moreno, S., and Taylor, S.S. (2010). Structure of yeast regulatory subunit: a glimpse into the evolution of PKA signaling. Structure *18*, 1471–1482.

Robert, X., and Gouet, P. (2014). Deciphering key features in protein structures with the new ENDscript server. Nucleic Acids Res. *42*, W320–W324.

Roelants, F.M., Breslow, D.K., Muir, A., Weissman, J.S., and Thorner, J. (2011). Protein kinase Ypk1 phosphorylates regulatory proteins Orm1 and Orm2 to control sphingolipid homeostasis in Saccharomyces cerevisiae. Proc. Natl. Acad. Sci. USA *108*, 19222–19227.

Ruprecht, B., Koch, H., Medard, G., Mundt, M., Kuster, B., and Lemeer, S. (2015). Comprehensive and reproducible phosphopeptide enrichment using iron immobilized metal ion affinity chromatography (Fe-IMAC) columns. Mol. Cell. Proteomics *14*, 205–215.

Santangelo, G.M. (2006). Glucose signaling in Saccharomyces cerevisiae. Microbiol. Mol. Biol. Rev. *70*, 253–282.

Sanz, P., Viana, R., and Garcia-Gimeno, M.A. (2016). AMPK in yeast: the SNF1 (sucrose non-fermenting 1) protein kinase complex. Exp Suppl *107* (*Suppl*), 353–374.

Schwämmle, V., and Jensen, O.N. (2018). VSClust: feature-based variance-sensitive clustering of omics data. Bioinformatics *34*, 2965–2972.

Senyilmaz, D., Virtue, S., Xu, X., Tan, C.Y., Griffin, J.L., Miller, A.K., Vidal-Puig, A., and Teleman, A.A. (2015). Regulation of mitochondrial morphology and function by stearoylation of TFR1. Nature *525*, 124–128.

Shabb, J.B. (2001). Physiological substrates of cAMP-dependent protein kinase. Chem. Rev. *101*, 2381–2411.

Shimobayashi, M., Oppliger, W., Moes, S., Jenö, P., and Hall, M.N. (2013). TORC1-regulated protein kinase Npr1 phosphorylates Orm to stimulate complex sphingolipid synthesis. Mol. Biol. Cell *24*, 870–881.

Silva, J.C., Gorenstein, M.V., Li, G.Z., Vissers, J.P., and Geromanos, S.J. (2006). Absolute quantification of proteins by LCMSE: a virtue of parallel MS acquisition. Mol. Cell. Proteomics *5*, 144–156.

Smyth, G.K. (2004). Linear models and empirical bayes methods for assessing differential expression in microarray experiments. Stat. Appl. Genet. Mol. Biol. *3*, Article3.

Spivak, M., Weston, J., Bottou, L., Käll, L., and Noble, W.S. (2009). Improvements to the percolator algorithm for Peptide identification from shotgun proteomics data sets. J. Proteome Res. *8*, 3737–3745.

Studer, R.A., Rodriguez-Mias, R.A., Haas, K.M., Hsu, J.I., Viéitez, C., Solé, C., Swaney, D.L., Stanford, L.B., Liachko, I., Böttcher, R., et al. (2016). Evolution of protein phosphorylation across 18 fungal species. Science *354*, 229–232.

Stukey, J.E., McDonough, V.M., and Martin, C.E. (1990). The OLE1 gene of Saccharomyces cerevisiae encodes the delta 9 fatty acid desaturase and can be functionally replaced by the rat stearoyl-CoA desaturase gene. J. Biol. Chem. *265*, 20144–20149.

Sutherland, C.M., Hawley, S.A., McCartney, R.R., Leech, A., Stark, M.J., Schmidt, M.C., and Hardie, D.G. (2003). Elm1p is one of three upstream kinases for the Saccharomyces cerevisiae SNF1 complex. Curr. Biol. *13*, 1299–1305.

Swinnen, E., Wanke, V., Roosen, J., Smets, B., Dubouloz, F., Pedruzzi, I., Cameroni, E., De Virgilio, C., and Winderickx, J. (2006). Rim15 and the crossroads of nutrient signalling pathways in Saccharomyces cerevisiae. Cell Div. *1*, 3.

Taus, T., Köcher, T., Pichler, P., Paschke, C., Schmidt, A., Henrich, C., and Mechtler, K. (2011). Universal and confident phosphorylation site localization using phosphoRS. J. Proteome Res. *10*, 5354–5362.

Topolska, M., Martínez-Montañés, F., and Ejsing, C.S. (2020). A simple and direct assay for monitoring fatty acid synthase activity and product-specificity by high-resolution mass spectrometry. Biomolecules *10*, 118.

Vance, J.E., and Vance, D.E. (2004). Phospholipid biosynthesis in mammalian cells. Biochem. Cell Biol. *82*, 113–128.

Wang, G., Wu, W.W., Zhang, Z., Masilamani, S., and Shen, R.F. (2009). Decoy methods for assessing false positives and false discovery rates in shotgun proteomics. Anal. Chem. *81*, 146–159.

Wanke, V., Pedruzzi, I., Cameroni, E., Dubouloz, F., and De Virgilio, C. (2005). Regulation of G0 entry by the Pho80-Pho85 cyclin-CDK complex. EMBO J. *24*, 4271–4278.

Wapinski, I., Pfeffer, A., Friedman, N., and Regev, A. (2007). Natural history and evolutionary principles of gene duplication in fungi. Nature *449*, 54–61.

Woods, A., Munday, M.R., Scott, J., Yang, X., Carlson, M., and Carling, D. (1994). Yeast SNF1 is functionally related to mammalian AMP-activated protein kinase and regulates acetyl-CoA carboxylase in vivo. J. Biol. Chem. *269*, 19509–19515.

Yu, Y., Sreenivas, A., Ostrander, D.B., and Carman, G.M. (2002). Phosphorylation of Saccharomyces cerevisiae choline kinase on Ser30 and Ser85 by protein kinase A regulates phosphatidylcholine synthesis by the CDP-choline pathway. J. Biol. Chem. *277*, 34978–34986.

Zechner, R., Zimmermann, R., Eichmann, T.O., Kohlwein, S.D., Haemmerle, G., Lass, A., and Madeo, F. (2012). FAT SIGNALS–lipases and lipolysis in lipid metabolism and signaling. Cell Metab. *15*, 279–291.

Zhu, J., and Thompson, C.B. (2019). Metabolic regulation of cell growth and proliferation. Nat. Rev. Mol. Cell Biol. *20*, 436–450.

## STAR★METHODS

### KEY RESOURCES TABLE

| REAGENT or RESOURCE | SOURCE | IDENTIFIER |
|---|---|---|
| Chemicals, Peptides, and Recombinant Proteins | | |
| Ammonium formate | Fluka | Cat# 17843 |
| Trypsin | Promega | Cat# V5111 |
| Chloroacetamide | Fluka | Cat# 22788 |
| Dimethyl sulfoxide (DMSO) | Biosolve | Cat# 4470602 |
| Ethyl acetate | Sigma-Aldrich | Cat# 650528 |
| Myo-inositol-1,2,3,4,5,6-D6 (98.8%) | CDN Isotopes | Cat# 68922-44-1 |
| L-methionine (methyl-D3, 98%) | Cambridge Isotope Laboratories, Inc. | Cat# DLM-431-1 |
| Choline bromide (D13, 98%) | Cambridge Isotope Laboratories, Inc. | Cat# DLM-3015-0.5 |
| L-serine ($^{13}C_3$, 99%;$^{15}N$, 99%) | Cambridge Isotope Laboratories, Inc. | Cat# CNLM-474-H-0.5 |
| D-glucose (U-13C6, 99%) | Cambridge Isotope Laboratories, Inc. | Cat# CLM-1396-10 |
| Methanol (LCMS grade) | Biosolve | Cat# 13687802BS |
| Chloroform (HPLC grade) | Rathburn | Cat# RH1009 |
| Water (LCMS grade) | VWR | Cat# 83645.320 |
| Water (ULC-MS grade) | Biosolve | Cat# 232141B1BS |
| 2-(Methylamino)ethanol | Sigma-Aldrich | Cat# 471445 |
| Geneticin (G-418) | Life Technologies Limited | Cat# 11811-031 |
| Phleomycin | InvivoGen | Cat# ant-ph-1 |
| Acetonitrile (ACN) (ULC-MS grade) | Biosolve | Cat# 1204101BS |
| Trifluoroacetic acid (TFA, ULC-MS grade) | Biosolve | Cat# 202341A8BS |
| Formic acid (99% ULC-MS grade) | Biosolve | Cat# 69141A8BS |
| Hydrochloric acid | Sigma-Aldrich | Cat# 30721 |
| n-Hexane | Rathburn | Cat# RH1034 |
| 2-propanol (LCMS grade) | Biosolve | Cat# 16267802BS |
| MS PhosphoMix 1 Light | Sigma-Aldrich | Cat# MSP1L |
| MS PhosphoMix 1 Heavy | Sigma-Aldrich | Cat# MSP1H |
| MS PhosphoMix 2 Light | Sigma-Aldrich | Cat# MSP2L |
| MS PhosphoMix 2 Heavy | Sigma-Aldrich | Cat# MSP2H |
| MS PhosphoMix 3 Light | Sigma-Aldrich | Cat# MSP3L |
| MS PhosphoMix 3 Heavy | Sigma-Aldrich | Cat# MSP3H |
| Hi3 *E. coli* ClpB standard | Waters Corporation | Cat# 186006012 |
| Cholesterol(+$^2H_7$) | Avanti Polar Lipids | Cat# 700041P |
| CE 18:1(+$^2H_7$) | Avanti Polar Lipids | Cat# 700185 |
| CE 10:0 | Sigma-Aldrich | Cat# C4633 |
| TAG 17:0/17:1/17:0(+$^2H_5$) | Avanti Polar Lipids | Cat# 860903 |
| DAG 17:0/17:0(+$^2H_5$) | Avanti Polar Lipids | Cat# 800854 |
| DAG 15:0/18:1(+$^2H_7$) | Avanti Polar Lipids | Cat# 791647 |
| LPA O-16:0 | Avanti Polar Lipids | Cat# 110683 |
| PA 15:0-18:1(+$^2H_7$) | Avanti Polar Lipids | Cat# 791642 |
| LPS 17:1 | Avanti Polar Lipids | Cat# 858141 |
| PS 17:0/14:1 | Avanti Polar Lipids | Cat# LM-1304 |

(*Continued on next page*)

*Continued*

| REAGENT or RESOURCE | SOURCE | IDENTIFIER |
|---|---|---|
| PS 15:0/18:1(+$^{2}H_{7}$) | Avanti Polar Lipids | Cat# 791639C |
| LPE O-16:0 | Avanti Polar Lipids | Cat# 110703 |
| PE 15:0/18:1(+$^{2}H_{7}$) | Avanti Polar Lipids | Cat# 791638 |
| PE O-20:0/20:0 | Avanti Polar Lipids | Cat# 999985C |
| LPC O-17:0 | Avanti Polar Lipids | Cat# 878101P |
| PC O-18:1/O-18:1 | Avanti Polar Lipids | Cat# 999989 |
| LPI 17:1 | Avanti Polar Lipids | Cat# 850103P |
| PI 15:0/18:1(+$^{2}H_{7}$) | Avanti Polar Lipids | Cat# 791641 |
| PG 15:0/18:1(+$^{2}H_{7}$) | Avanti Polar Lipids | Cat# 791640 |
| CL 14:0/14:0/14:0/14:0 | Avanti Polar Lipids | Cat# 7103320 |
| Cer 18:1;2/17:0;1 | Avanti Polar Lipids | Cat# 860817 |
| CDPDAG 17:0-18:1 | Avanti Polar Lipids | Cat# 110850 |
| NEFA 16:0(+$^{2}H_{4}$) | Larodan Fine Chemicals | Cat# 71-1604 |
| 19:0-CoA | Avanti Polar Lipids | Cat# 870738 |
| IPC 18:0;2/26:0 | Purified in house | N/A |
| MIPC 18:0;2/26:0 | Purified in house | N/A |
| $M(IP)_2C$ 18:0;2/26:0 | Purified in house | N/A |
| Potassium dihydrogen phosphate | Merck | Cat# 1.04873.1000 |
| di-potassium hydrogen phosphate | Merck | Cat# 1.05104.1000 |
| Iron(III) chloride hexahydrate ($FeCl_3$) | Sigma-Aldrich | Cat# 236489 |
| Nicotinamide adenine dinucleotide phosphate (NADPH) | Roche Diagnostics | Cat# 10107824001 |
| Lithium acetate | Thermo Fischer | Cat# A17921 |
| Polyethylene glycol 4000 | Roth | Cat# 0156.3 |
| cOmplete, Mini, EDTA-free protease inhibitor cocktail | Roche Diagnostics | Cat# 11836170001 |
| PhosSTOP, phosphatase inhibitor cocktail | Roche Diagnostics | Cat# 04906845001 |
| Tris(2-carboxyethyl)phosphine | Sigma-Aldrich | Cat# 646547 |
| Triethylammonium bicarbonate buffer (TEAB) | Fluka | Cat# 17902 |
| Sodium deoxycholate (SDC) | Sigma-Aldrich | Cat# 30968 |
| Glucose | Sigma-Aldrich | Cat# G7021 |
| Agar, granulated | Difco | Cat# 214530 |
| Yeast Extract | Difco | Cat# 210929 |
| Bacto Peptone | Difco | Cat# 211677 |
| Ethylenediamine tetraacetic acid disodium salt dihydrate (EDTA) | Roth | Cat# 8043.2 |
| L-cysteine | Sigma-Aldrich | Cat# 168149 |
| Malonyl-$^{13}C_3$ coenzyme A | Sigma-Aldrich | Cat# 655759 |
| Acetyl-CoA | Sigma-Aldrich | Cat# A2181 |
| Glycerol 85% | Merck | Cat# 1.04094.2500 |
| Ethanol 96% | VWR Chemicals | Cat# 20824.365 |
| Bovine serum albumin (fatty acid free) | Sigma-Aldrich | Cat# A7030-50G |
| Critical Commercial Assays | | |
| BCA Protein Assay Kit | ThermoFisher Scientific | Cat# 23225 |
| Deposited Data | | |
| Proteomics data | This paper | Deposited to PRIDE with dataset identifier PXD015281. |
| Experimental Models: Organisms/Strains | | |
| BY4742 (*MATα; his3Δ1; leu2Δ0; lys2Δ0; ura3Δ0*) | EUROSCARF | N/A |
| [BY4742] *bleMX::cds1*$^{S40A,S42A,T44A}$ | This paper | N/A |

(*Continued on next page*)

*Continued*

| REAGENT or RESOURCE | SOURCE | IDENTIFIER |
|---|---|---|
| [BY4742] *bleMX::CDS1* | This paper | N/A |
| [BY4742] *FAS2-GFP::kanMX* | This paper | N/A |
| [BY4742] *fas2*$^{S1440E,S1640E,S1827E}$*-GFP::kanMX::bleMX* | This paper | N/A |
| [BY4742] *FAS2::bleMX* | This paper | N/A |
| [BY4742] *fas2*$^{S1440E,S1640E,S1827E}$*::bleMX* | This paper | N/A |
| [BY4742] *fas2*$^{S1440A,S1640A,S1827A}$*::bleMX* | This paper | N/A |
| [BY4742] *bleMX::CHO1* | This paper | N/A |
| [BY4742] *bleMX::cho1*$^{S4E,Y32E,S34E,S46E,S47E,T53E,T54E}$ | This paper | N/A |
| [BY4742] *bleMX::cho1*$^{S4A,Y32A,S34A,S46A,S47A,T53A,T54A}$ | This paper | N/A |
| [BY4742] *bleMX::LCB5* | This paper | N/A |
| [BY4742] *bleMX::lcb5*$^{S54E,S55E,S60E,S63E}$ | This paper | N/A |
| [BY4742] *bleMX::lcb5*$^{S38A,S39A,T42A,S52A,S54A,S55A,S60A,T62A,S63A}$ | This paper | N/A |
| [BY4742] *bleMX::lcb5*$^{S201A,S202A}$ | This paper | N/A |
| [BY4742] *bleMX::lcb5*$^{S201E,S202E}$ | This paper | N/A |
| [BY4742] *bleMX::ORM2* | This paper | N/A |
| [BY4742] *bleMX::orm2*$^{T5A,S9A,S15A,T18A}$ | This paper | N/A |
| [BY4742] *bleMX::orm2*$^{T5E,S9E,S15E,T18E}$ | This paper | N/A |
| [BY4742] *elo1Δ::kanMX* | EUROSCARF | N/A |
| [BY4742] *elo2Δ::kanMX* | EUROSCARF | N/A |
| [BY4742] *elo1Δ::URA3; fas2*$^{S1440E,S1640E,S1827E}$*::bleMX* | This paper | N/A |
| [BY4742] *elo2Δ::URA3; fas2*$^{S1440E,S1640E,S1827E}$*::bleMX* | This paper | N/A |
| Oligonucleotides | | |
| See Table S5 for list of primers | This paper | N/A |
| Recombinant DNA | | |
| See Table S6 for list of gBlocks® | Integrated DNA Technologies | N/A |
| Software and Algorithms | | |
| Proteome Discoverer v.2.1.1.21 | Thermo Fisher Scientific | N/A |
| Mascot server, version 2.4 | Matrix Science | N/A |
| Progenesis QI for proteomics v2.0 | Nonlinear Dynamics / Waters | N/A |
| R-based Shiny app for statistical analysis | Schwämmle and Jensen, 2018 | http://computproteomics.bmb.sdu.dk/Apps/VSClust |
| Percolator algorithm | Käll et al., 2007 | N/A |
| ptmRS algorithm | Taus et al., 2011 | N/A |
| Meme Suite 5.0.5 | Cheng et al., 2018 | http://meme-suite.org/tools/momo |
| NetworKIN 3.0 | Horn et al., 2014 | http://networkin.info/ |
| Venny 2.1 | N/A | https://bioinfogp.cnb.csic.es/tools/venny/index.html |
| T-coffee | Di Tommaso et al., 2011 | http://tcoffee.crg.cat/apps/tcoffee/do:expresso |
| ESPript 3.0 | Robert and Gouet, 2014 | http://espript.ibcp.fr/ESPript/ESPript/ |
| Cn3D (v4.3.1) | N/A | https://www.ncbi.nlm.nih.gov/Structure/CN3D/cn3d.shtml |
| Clustvis | Metsalu and Vilo, 2015 | https://biit.cs.ut.ee/clustvis/ |
| ALEX$^{123}$ | Ellis et al., 2018; Husen et al., 2013; Pauling et al., 2017 | http://mslipidomics.info/contents/?page_id=525 |
| Other | | |
| TriVersa NanoMate | Advion Biosciences | N/A |
| Orbitrap Fusion Tribrid mass spectrometer | Thermo Fisher Scientific | N/A |

(*Continued on next page*)

*Continued*

| REAGENT or RESOURCE | SOURCE | IDENTIFIER |
|---|---|---|
| Ozone generator | Paine et al., 2018 | N/A |
| Dionex Ultimate 3000 nano UPLC system | Thermo Fisher Scientific | N/A |
| Oasis HMB 3cc, 60mg | Waters Corporation | Cat# WAT094226 |
| ProPac IMAC-10 column (2 mm x 50 mm) | Thermo Fisher Scientific | Cat# 063272 |
| XBridge BEH C18 (300 μm x 50 mm, 5 μm particle size) | Waters Corporation | Cat# 186003682 |
| Symmetry C18 trap column (180 μm x 20 mm, 5 μm particle size) | Waters Corporation | Cat# 186007500 |
| HSS T3 C18 column (75 μm x 250 mm; 1.8 μm particle size) | Waters Corporation | Cat# 186007474 |
| Biochrom 30 amino acid analyzer | Biochrom | Cat# 80-6000-50 |
| Bioruptor UCD-200 | Diagenode | N/A |
| Mini-BeadBeater-24 | BioSpec Products | Cat# 112011 |
| 6x8 Replica plater | Sigma-Aldrich | Cat# R2383-1EA |

## RESOURCE AVAILABILITY

### Lead Contact

Further information and requests for resources and reagents should be directed to and will be fulfilled by the Lead Contact, Christer S. Ejsing (cse@bmb.sdu.dk).

### Materials Availability

All reagents generated in this study are available from the Lead Contact without restriction.

### Data and Code Availability

The phosphoproteomics and proteomics data are provided in Tables S1 and S2, respectively, and the lipidomics data in Table S3. Original LC-MS phosphoproteomics data have been deposited to PRIDE with dataset identifier: PXD015281.

## EXPERIMENTAL MODEL AND SUBJECT DETAILS

### Yeast strains and growth conditions

*Saccharomyces cerevisiae* BY4742 (*MATα his3Δ1 leu2Δ0 lys2Δ0 ura3Δ0*) (EUROSCARF, Frankfurt am Main, Germany) and isogenic mutant strains are listed in the Key Resources Table. Phosphosite mutant strains and control strains were generated by homologous recombination of custom-designed gBlocks® gene fragments carrying the *Klebsiella pneumoniae* bleMX resistance cassette (Gueldener et al., 2002). Transformed yeast cells were plated on YPD plates containing 20 μg phleomycin/ml (pH 7) for selection of viable transformants. Correct integration of the desired mutations and the resistance marker gene was verified by sequencing of PCR amplified DNA fragments.

## METHOD DETAILS

### Sample preparation for phosphoproteomics analysis of the yeast life cycle

Wild-type BY4742 was cultured in liquid YPD medium and sampled as previously described (Casanovas et al., 2015). In short, cells were batch cultured in three biological replicates at 30°C for 48 hours cells with a starting $OD_{600}$ of 0.2. Cells were harvested at the time points 6, 12, 20 and 48 hours corresponding to the exponential growth phase, the diauxic shift, the post-diauxic growth phase, and the stationary phase, respectively. Collected cell pellets (~25 ODu) were resuspended in lysis buffer (50 mM triethylammonium bicarbonate buffer, 1% w/v SDC, 1 x EDTA-free protease inhibitor cocktail (Roche Diagnostics), 1 x phosphatase inhibitor cocktail (Roche Diagnostics)) and lysed with glass beads using a cell disruptor (Mini-Beadbeater, Biospec Products) at 4°C. An aliquot of the cell lysate was withdrawn for determination of protein concentration using the BCA assay (ThermoFisher Scientific). Samples were then incubated for 10 min at 80°C after addition of tris(2-carboxyethyl)phosphine and chloroacetamide to a final concentration of 10 mM and 40 mM, respectively, and subsequently sonicated using a Bioruptor sonication system (Diagenode). Proteins were digested with trypsin using the ISD:SDC(PT) protocol (León et al., 2013) with minor modifications. In short, 550 μg of protein were added trypsin (Promega) at 1:50 w/w enzyme-to-protein ratio, adjusted to 500 μL with 1% w/v SDC and incubated for 7 hours at 37°C. Following incubation, 57 μL of DMSO, 1 mL of ethyl acetate and 15 μL of 20% v/v TFA were added to the digest and SDC was removed by phase transfer. After centrifugation (15,000 g, 5 min, 10°C) the aqueous phase, containing the peptides, was collected. An aliquot (30 μL) was withdrawn for proteomic analysis and the remaining sample was desalted using Oasis HLB

cartridges (Waters, Milford, MA). Briefly, cartridges were conditioned with ACN and equilibrated with 0.1% v/v TFA. Samples were loaded in 0.1% v/v TFA, washed with 0.1% v/v TFA and eluted with 30% v/v ACN, 0.1% v/v TFA followed by 60% v/v ACN, 0.1% v/v TFA. Desalted peptides were dried by vacuum centrifugation and stored at −80°C until phosphopeptide enrichment. The peptide concentration in the resulting extracts was determined by amino acid analysis as described (Højrup, 2015) using a Biochrom 30 amino acid analyzer (Biochrom).

### Phosphopeptide enrichment

Peptides were reconstituted in 50 μL of 50 % v/v ACN, 0.1% v/v TFA containing a mixture of isotopically labeled phosphopeptide standards (80 fmol of each peptide; MS Phosphomix 1-3 Heavy, Sigma). Phosphopeptide enrichment was carried out using an Fe-immobilized metal affinity chromatography (IMAC) column (2 × 50 mm, ProPac IMAC-10, Thermo Fisher Scientific) connected to an Ultimate 3000 HPLC system (Dionex/Thermo Scientific). The column was charged offline with iron essentially as described in Ruprecht et al. (2015), with minor modifications. In short, the column was rinsed with 3 column volumes of 0.1% v/v formic acid, charged with 3 column volumes of 25 mM $FeCl_3$, 100 mM acetic acid and flushed with 20 column volumes of 0.1% v/v formic acid. The sample was loaded for 4 min at 50 μL/min with 50% v/v ACN, 0.05% v/v TFA, followed by washing out of the unbound peptides for 2 min at a higher flowrate of 200 μL/min. Elution of the phosphopeptides was achieved with 50% ACN (pH 10) in water (20 mM $NH_4OH$) for 2 min at 200 μL/min followed by 2 min of 20 mM $NH_4OH$ (pH 10) and re-equilibration of the column for 8 min at 200 μL/min with 50% v/v ACN, 0.05% v/v TFA The phosphopeptide fraction was collected according to the UV signal (280 nm) and the retention times of phosphopeptide standards determined in preliminary runs. A mixture of (non-labeled) phosphopeptide standards (80 fmol of each peptide; MS Phosphomix 1-3 Light, Sigma), analogous to the mixture added before phosphopeptide enrichment, was spiked into the eluate of each sample to assess phosphopeptide recovery. Samples were subsequently dried and stored at −80°C until analyzed.

### LC-MS/MS analysis of (phospho)peptides

Peptides were analyzed by LC-MS/MS using a Dionex Ultimate 3000 nano UPLC system coupled to an Orbitrap Fusion mass spectrometer (both from Thermo Scientific) using a TriVersa NanoMate (Advion Biosciences) nanoelectrospray source. For proteome analysis, 1.5 μg of peptides were analyzed by online 2D (high pH reversed phase/low pH reversed phase) LC-MS/MS. Protein digests were first mixed with 100 fmol of the Hi3 synthetic *E. coli* ClpB internal protein standard (Waters Corporation, Milford, MA, USA) and then trapped on the first dimension XBridge BEH C18 reversed phase column (300 μm x 50 mm, 5 μm particle size; Waters) at 2 μL/min with 3% ACN in 20 mM ammonium formate (pH 10). To generate five fractions, discrete two-minute steps at 2 μL/min of respectively 11.5%, 15.0%, 18.0%, 21.5% and 50.0% ACN were used. An eluting fraction was online acidified and diluted 10-fold with 0.1% TFA in water at 20 μL/min and trapped on a Symmetry C18 trapping column (180 μm x 20 mm, 5 μm particle size; Waters). Each fraction was separated with a C18 HSS-T3 reversed phase analytical column (75 μm x 250 mm, 1.8 μm particle size; Waters) at 350 nl/min using a 30 min gradient of 6%–28% ACN with 0.1% formic acid. For each subsequent fraction the gradient start and end-points were increased with 2%. On the other hand, for phosphopeptide analysis, the enriched phosphopeptide fraction was reconstituted in 10% DMSO, 0.5% TFA and one fourth of the fraction was analyzed by LC-MS/MS. Peptides were trapped on a 2 cm Symmetry C18 column (180 μm, 5 μm particle size; Waters) with 0.1% TFA in water for 2 min at 15 μL/min and separated with a 25 cm C18 HSS-T3 column (75 μm, 1.8 μm particle size; Waters) at 350 nl/min using a 90 min gradient of 4%–37% ACN with 0.1% formic acid.

In all analyses, eluting peptides were ionized at 1.7 kV using a TriVersa NanoMate coupled to an Orbitrap Fusion instrument with the source capillary set at 275°C. The mass spectrometer was operated in data-dependent mode at a target mass resolution of 120,000 (at *m/z* 200). The scan range of each survey scan was *m/z* 350-1500 with a 5E5 ion count target and quadrupole wide-isolation window on. Tandem MS was performed by isolation at 0.7 Th with the quadrupole, HCD fragmentation with normalized collision energy of 30%, and rapid scan MS analysis in the ion trap. For proteome analysis, the MS/MS ion count target was set to 1E4 with a maximum injection time of 35 ms. Top speed mode was selected with a maximum cycle of 1.5 s, only selecting precursors with charge state 2-6 and a dynamic exclusion duration of 20 s with a 5 ppm tolerance around the selected precursor. For phosphopeptide analysis, the MS/MS ion count target and maximum injection time were set according to the 'Universal Method', respectively 1E2 and 300 ms. The instrument was run in top speed mode with maximum 3 s cycles and only precursors with charge state 2-7 were selected for MS/MS. The dynamic exclusion duration was set to 30 s with a 5 ppm tolerance around the precursor.

### Peptide identification

The fragmentation spectra were searched using the search engine Mascot against a customized database containing the yeast ORF database (*Saccharomyces* Genome Database; release January 13, 2015; 6713 entries) and additional entries including phosphopeptide standards and common contaminants (6783 entries in total). The search was facilitated through the Proteome Discoverer software (v2.1, Thermo Scientific) using the following parameters: trypsin, maximum 2 missed cleavages, 10 ppm precursor mass tolerance, 0.35 Da fragment mass tolerance, cysteine carbamidomethylation as a fixed modification and acetylation of protein N-terminal, and oxidation of methionine as dynamic modifications. The phosphorylation of serine, threonine or tyrosine was only considered as dynamic modification for samples subjected to phosphopeptide enrichment. The localization probability for each

phosphorylation site was calculated using ptmRS (Taus et al., 2011). Peptide identifications were filtered at 1% false discovery rate on peptide level using Percolator (Käll et al., 2007; Spivak et al., 2009).

### Spot assay

Yeast strains were pre-cultured for 48 hours in liquid YPD. Cell suspensions were diluted to an $OD_{600}$ of 1 and further serial diluted (10-fold) in YP medium without glucose. Cell suspensions were spotted using a 6x8 replica plater (Sigma-Aldrich) onto YP agar plates containing either 2% glucose (YPD), 3% glycerol (YPG) or 2% ethanol (YPE). Plates were incubated at 30°C and spot density was evaluated after 2-4 days.

### Lipidomics flux analysis

Yeast strains were pre-cultured in 10 mL liquid YPD at 30°C for 48 hours. Cell suspensions were subsequently diluted to an $OD_{600}$ of 0.2 in 10 mL in YPD or YPG medium. At an $OD_{600}$ of 0.8-1.0 the cell suspensions were diluted to an $OD_{600}$ of 0.0005 in 10 mL YPD or to 0.1 in YPG, and cultured overnight (~14 hours). The cell suspensions were then diluted again to an $OD_{600}$ of 0.25 in 10 mL YPD or YPG medium. At an $OD_{600}$ of ~1, 5 mL cell suspensions were spiked with 146 μL tracer cocktail containing 4.6 mM $^{13}C_3{}^{15}N$-serine, 0.66 mM $^2H_3$-methionine, 0.22 mM $^2H_6$-inositol and 0.54 mM $^2H_{13}$-choline bromide. After 90 minutes in YPD and 180 min in YPG, the cell suspensions were centrifuged, washed with 4°C deionized water, frozen in liquid nitrogen and stored at −80°C. Preliminary experiments showed that the incorporation of the tracers did not reach steady-state when using these labeling times.

In-depth lipidome analysis was performed as described previously (Almeida et al., 2015; Ejsing et al., 2009). In short, yeast cell pellets (~5 ODu) were resuspended in 1 mL of 155 mM ammonium formate and lysed at 4°C with 400 μL of acid-washed glass beads using a Mini-Beadbeater (Biospec). Lysates corresponding with 0.4 ODu were spiked with 30 μL of internal standard mixture providing a spike of 1000 pmol cholesterol(+$^2H_7$), 125 pmol CE 18:1(+$^2H_7$), 30 pmol TAG 17:0/17:1/17:0(+$^2H_5$), 25 pmol DAG 15:0/18:1(+$^2H_7$), 20 pmol LPA O-16:0, 62 pmol PA 15:0-18:1(+$^2H_7$), 40 pmol LPS 17:1, 60 pmol PS 15:0/18:1(+$^2H_7$), 80 pmol LPE O-16:0, 110 pmol PE O-20:0/O-20:0, 50 pmol LPC O-17:0, 70 pmol PC O-18:1/O-18:1, 30 pmol LPI 17:1, 33 pmol PI 15:0/18:1(+$^2H_7$), 35 pmol PG 15:0/18:1(+$^2H_7$), 40 pmol CL 14:0/14:0/14:0/14:0, 90 pmol Cer 18:1;2/17:0;1, 40 pmol CDPDAG 17:0/18:1, 65 pmol IPC 18:0;2/26:0, 50 pmol MIPC 18:0;2/26:0, 120 pmol $M(IP)_2C$ 18:0;2/26:0 and 50 pmol NEFA 16:0(+$^2H_4$). The samples were subsequently subjected to two-step lipid extraction (Ejsing et al., 2009) and lipid extracts were vacuum evaporated. Finally, the lipid extracts were reconstituted in 100 μL chloroform/methanol (1:2; v/v) and analyzed by $MS^{ALL}$ (Almeida et al., 2015) using an Orbitrap Fusion Tribrid (Thermo Fisher Scientific) equipped with a TriVersa NanoMate robotic nanoflow ion source (Advion Biosciences). Lipid identification and quantification was done using $ALEX^{123}$ software (Ellis et al., 2018; Husen et al., 2013; Pauling et al., 2017). FA chains of reported lipid molecules identified by manual inspection of high-resolution $FTMS^2$ data.

### Flow cytometry

Cells were resuspended in phosphate-buffered saline and analyzed on an LSRFortessa flow cytometer (BD BioSciences). Flow cytometry data was analyzed using FlowJo software (BD BioSciences) and fluorescent levels of cells were quantified by their means.

### *In vivo* FAS activity and double bond position analysis

BY4742 and *fas2*$^{3E}$ were pre-cultured in 10 mL liquid YPD at 30°C for 48 hr. Cell suspensions were subsequently diluted to an $OD_{600}$ of 0.2 in 10 mL YPD. At an $OD_{600}$ of ~1, the cell suspensions were diluted to an $OD_{600}$ of 0.001 in 10 mL YPD medium and cultured overnight. Next morning, the cell suspensions were diluted to an $OD_{600}$ of 0.1 in 10 mL YPD. At an $OD_{600}$ of ~0.6, 5 mL of the cell suspensions were centrifuged and the resulting cell pellets were washed once with 5 mL prewarmed YP medium. The cells were then resuspended in 5 mL of prewarmed YP containing 2% $^{13}C_6$-glucose and cultured for 90 minutes at 30°C. Cells were subsequently harvested, washed once with 4°C deionized water, frozen in liquid nitrogen, and stored at −80°C.

Total FA analysis of the collected samples were carried out by high-resolution shotgun lipidomics analysis, as described recently (Gallego et al., 2018). Cell lysates corresponding to 0.1 ODu were transferred to 1.1 mL glass vials fitted with PTFE-lined screw caps (La-Pha-Pack GmbH), 864.5 pmol of internal standard PI 15:0/18:1(+$^2H_7$) was added and samples were vacuum evaporated for 30 min. Samples were then dissolved in 80 μL of ACN/water/15% HCl (10:1:2, v/v/v) and placed in a ThermoMixer (Eppendorf) for 5 hours (90°C, 750 rpm). After cooling the samples for 5 min, the resulting fatty acids were extracted at 4°C with 180 μL of *n*-hexane by mixing for 10 min followed by centrifugation for 5 min at 1000 g. The fatty acid extraction with *n*-hexane was repeated, and both extracts were collected in a new glass vial and vacuum evaporated.

For mass spectrometry analysis, extracts were dissolved in 150 μL chloroform/methanol/2-propanol (1:2:4 v/v/v) containing 0.75 mM ammonium formate and loaded in a 96-well plate (Eppendorf, Hamburg, Germany). Ten μL of the extracts were infused with the robotic nanoflow ion source TriVersa NanoMate (Advion Biosciences) and analyzed in negative ion mode using an Orbitrap Fusion Tribrid (Thermo Fisher Scientific) coupled to an ozone generator that delivers ozone into the ion trap collision cell of the instrument (Paine et al., 2018). Quantitative monitoring of deprotonated FA analytes was carried out by high-resolution FTMS analysis of the *m/z* ranges 150-420 and 200-1200 using a max injection time of 100 ms, automated gain control for an ion target of 1e5, three microscans, and a target resolution setting of 500,000 (Gallego et al., 2018). Quantitative monitoring of FA 18:1 double bond isomers was carried out by OzID-based $FTMS^2$ analysis. To this end, the precursor ion *m/z* 281.25, corresponding to deprotonated FA 18:1, was selected using a quadrupole ion isolation width of 1.6 amu, transferred into the ion trap collision cell, reacted with ozone for 1 s

together with a supplemental collision energy of 20%, followed FTMS analysis of OzID fragments using a max injection time of 1000 ms, automated gain control for an ion target of 1e5, two microscans, and a target resolution setting of 120,000. Lipid identification and quantification was done using ALEX$^{123}$ software (Ellis et al., 2018; Husen et al., 2013; Pauling et al., 2017).

### *In vitro* FAS activity analysis

FAS activity was assayed using $^{13}C_3$-malonyl-CoA and high-resolution mass spectrometry as recently described (Topolska et al., 2020). In short, BY4742 and *fas2*$^{3E}$ cells were grown to an $OD_{600}$ of ~2.5 and 50 ODu of cells were harvested (3000 g, 3 min) and washed with sterile, deionized water. The cell pellet was resuspended in 500 μL of ice-cold 100 mM potassium phosphate (pH 7.4) containing 1 mM PMSF. Lysis was performed with glass beads in a Mini-Beadbeater (with six cycles of 1 min and 1 min of cooling on ice between cycles). The lysate was centrifuged for 3 minutes at 3000 g and at 4°C. The supernatants were transferred to new Eppendorf tubes and centrifuged for 20 min at 20000 g at 4°C to produce a cytosolic fraction enriched for the FAS complex and depleted of cellular membranes. Next, the FAS-catalyzed reaction was carried out for 10 min at room temperature in a reaction mixture (total volume of 500 μL) containing 0.1 M potassium phosphate (pH 6.5), 2 mM EDTA, 10 mM cysteine, 0.2 mM NADPH, 0.05 mM acetyl-CoA, 0.15 mg BSA, 450 μg of total protein extract, and 0.08 mM $^{13}C_3$-malonyl-CoA. For detection of *de novo* synthesized $^{13}$C-labeled FAs, 200 μL of the reaction mixture was transferred to a 1.1 mL glass vials fitted with PTFE-lined screw caps and spiked with 200 pmol 19:0-CoA. Samples were mixed with 100 μL 5 M HCl and incubated for 2.5 hours at 90°C in a ThermoMixer (Eppendorf) at 750 rpm. After the hydrolysis step, samples were kept on ice for 10 min and NEFAs were then extracted twice with 700 μL of *n*-hexane. Analysis of total FA by high-resolution FTMS was performed as described in the previous section (without OzID-based FTMS$^2$ analysis).

## QUANTIFICATION AND STATISTICAL ANALYSIS

### Protein and phosphopeptide quantification

Peptide abundance was estimated by a label-free quantification approach using the Progenesis QI for proteomics software (v2.0, Nonlinear Dynamics Limited, Waters). Briefly, the LC-MS/MS maps of each fraction (proteome) or sample (phosphoproteome) across the all samples were aligned and peptides were quantified based on peak areas of precursor ions (FTMS$^1$). The MS/MS data associated to each precursor ion were exported from Progenesis as MGF files (Mascot generic format) and used for peptide identification with the Proteome Discoverer software as indicated above. The peptide identifications were re-imported into Progenesis QI and matched to the corresponding feature across the different runs. Absolute protein abundance (fmol on-column) was estimated by the Hi3-based quantification method (Silva et al., 2006) using the known amount of spiked-in Hi3 ClpB protein standard. To determine the expression level (fmol/μg), the $M_w$ of each protein was used to calculate the total on-column protein amount (μg) for each sample, followed by dividing individual protein fmol on-column amounts by the median total on-column protein amount across all samples. Following protein quantification, the results were further filtered to 1% false discovery rate on protein level by applying the standard target-decoy approach correcting for the use of separate protein target-decoy search results (Wang et al., 2009) as obtained using Proteome Discoverer.

Standard median normalization was applied to quantified proteins and phosphopeptides. The normalized phosphopeptide abundances were corrected based on matching protein accession, using the average normalized protein abundance per time point. Phosphopeptides that did not have a corresponding protein match were not included in further analyses. To aid comparative visualization, phosphopeptide abundances were standardized using z-scoring. The z-score was calculated for individual phosphopeptides using the equation: $z\text{-score} = (x_i - AV(x_i))/SD(x_i)]$; where $x_i$ denotes abundances of an individual phosphopeptide, $AV(x_i)$ is the average of all $x_i$ abundances, and $SD(x_i)$ is the standard deviation of all $x_i$ abundances.

### Statistical analysis of phosphoproteomics data

Protein and peptide abundance values were log2 transformed followed by statistical analyses using the limma R package contained in the online VSClust application (Schwämmle and Jensen, 2018), performing moderated unpaired t tests using the eBayes module (Smyth, 2004). The results were corrected for multiple hypothesis testing and q-values below 0.01 were considered statistically significant.

### Bioinformatic analysis of phosphoproteomics data

Phosphopeptide sequences harboring single p-sites were grouped by highest abundance at each growth phase, centralized to the modified residue and searched for overrepresented phosphorylation motifs using the MoMo algorithm (min. occurrences = 20; significance = 0.000001) (Cheng et al., 2018). Predictions of kinases phosphorylating the sites matching the obtained motifs were obtained from the NetworKIN algorithm using default settings (Horn et al., 2014).

### Phylogenetic analysis

The evolutionary conservation of mutated p-sites in selected lipid metabolic proteins was investigated by retrieving orthologous protein sequences belonging to 23 ascomycete taxa from the fungal orthogroups repository (Wapinski et al., 2007). Multiple sequence alignment of *S. cerevisiae* and other ascomycetes was performed using the online available programs T-Coffee and ESPript 3.0 (Di Tommaso et al., 2011; Robert and Gouet, 2014).

### Lipid abundances from mass spectrometric data

Lipid identification and quantification was performed using the ALEX$^{123}$ software framework and SAS 9.4 (SAS Institute) (Ellis et al., 2018; Husen et al., 2013). Briefly, intensities of lipid species monitored by FTMS were quantified by normalization to the respective internal lipid standard and subsequent multiplication by the amount of the respective lipid standard. Data shown in bar graphs are represented as mean mol% per all lipids or lipid class, and dots individual measurements of 2-3 biological replicates. Principal component analysis was carried out using Clustvis (Metsalu and Vilo, 2015). Data were visualized using Tableau Desktop (Tableau Software).